HOKKAIDO UNIVERSITY

Title	Dense magnetotelluric imaging of the Akan Caldera (Hokkaido, Japan): insights into its magma plumbing system and caldera-forming reservoir
Author(s)	Inoue, Tomohiro; Hashimoto, Takeshi; Aizawa, Koki et al.
Citation	Earth, Planets and Space, 78(1), 79 https://doi.org/10.1186/s40623-026-02398-8
Issue Date	2026-03-16
Doc URL	https://hdl.handle.net/2115/100326
Rights(URL)	https://creativecommons.org/licenses/by/4.0/
Type	journal article
File Information	s40623-026-02398-8.pdf

Hokkaido University Collection of Scholarly and Academic Papers : HUSCAP

Earth, Planets and Space

FULL PAPER Open Access

Dense magnetotelluric imaging of the Akan Caldera (Hokkaido, Japan): insights into its magma plumbing system and caldera-forming reservoir

Tomohiro Inoue[1,2,3*], Takeshi Hashimoto[4], Koki Aizawa[2], Hiroshi Ichihara[5], Ryo Tanaka[4] and Yusuke Yamaya[6]

Abstract

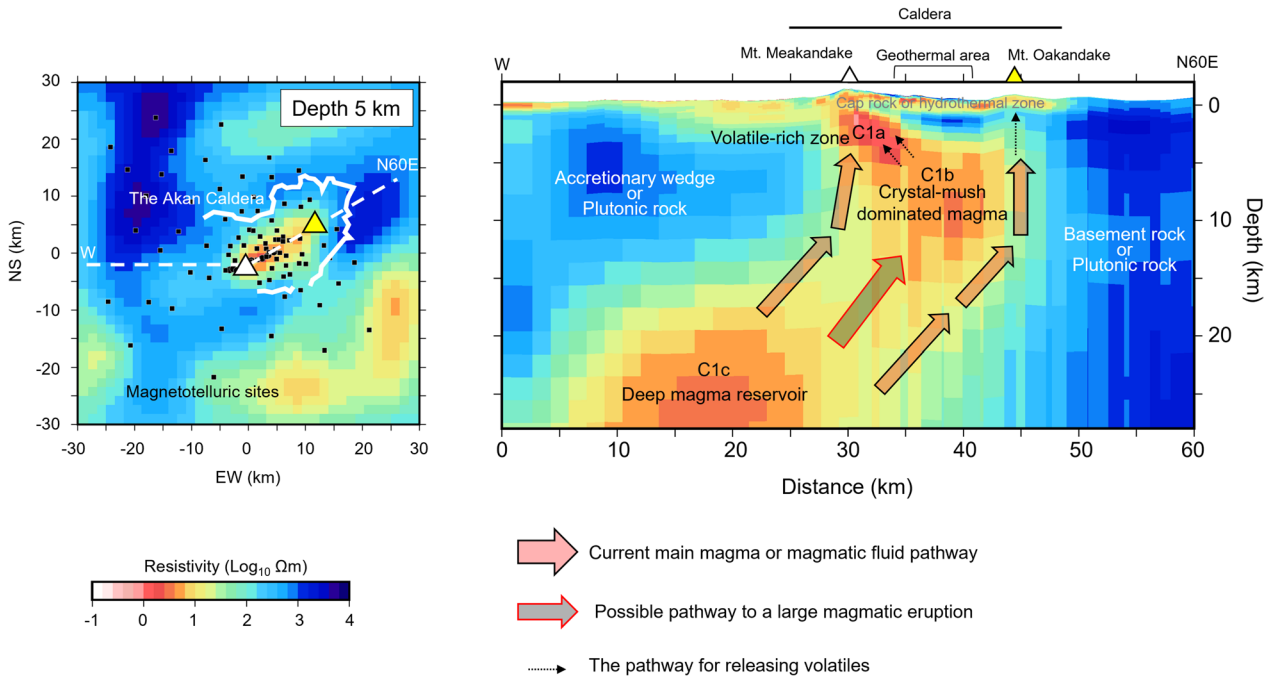
To investigate the magma plumbing system beneath the Akan Caldera (Hokkaido, Japan), we conducted broadband magnetotelluric surveys and imaged its three-dimensional resistivity structure to a depth of approximately 30 km. The caldera hosts post-caldera volcanoes, including Mt. Meakandake and Mt. Oakandake, which have recently shown ground inflation and heightened deep low-frequency seismicity. Our main finding is a prominent, westward-dipping conductive column beneath the caldera. This conductor is interpreted as the magma plumbing system of the Akan Caldera, comprising three distinct components, for which we estimated volumes based on the spatial extent of the conductive region: (1) the volatile-rich zone at depths of 2–5 km (~ 10 km^3, < 10 Ωm), (2) a mushy dacitic magma reservoir beneath the caldera center at depths of 3–15 km (~ 500 km^3, < 10 Ωm), and (3) a deeper basaltic magma reservoir to the west at depths of 15–30 km (~ 4500 km^3, < 70 Ωm). The active volcanoes, deformation sources, and earthquake hypocenters are located above or near the conductor edges (2), suggesting that magmatic fluids from the deeper western source (3) preferentially ascend along the column edges. A distinctive feature of the caldera is the flattened upper boundary of conductor (2), which is associated with sill-shaped ground inflation. This geometry may indicate the potential to store large volume of mushy magma, which could become eruptible if magma is directly supplied from greater depths. This study provides new insights into the magma plumbing system beneath the Akan Caldera and enhances our understanding of the mechanisms underlying its volcanic activity.

Keywords Broadband magnetotelluric survey, The Akan Caldera, Magma plumbing system, Magma reservoir, Caldera-forming eruption, 3D resistivity model

*Correspondence:
Tomohiro Inoue
tomohiro.inoue@aist.go.jp
Full list of author information is available at the end of the article

© The Author(s) 2026. **Open Access** This article is licensed under a Creative Commons Attribution 4.0 International License, which permits use, sharing, adaptation, distribution and reproduction in any medium or format, as long as you give appropriate credit to the original author(s) and the source, provide a link to the Creative Commons licence, and indicate if changes were made. The images or other third party material in this article are included in the article's Creative Commons licence, unless indicated otherwise in a credit line to the material. If material is not included in the article's Creative Commons licence and your intended use is not permitted by statutory regulation or exceeds the permitted use, you will need to obtain permission directly from the copyright holder. To view a copy of this licence, visit http://creativecommons.org/licenses/by/4.0/.

Graphical abstract



1 Introduction

The Akan Caldera is located at the southern end of the Akan–Shiretoko Volcanic Chain in eastern Hokkaido, Japan (Fig. 1a). The caldera has a complex east–west elongated shape (24 × 13 km in diameter) and was formed by at least three major eruptions (Hasegawa et al. 2009, 2012). These large eruptions (Volcanic Explosivity Index: VEI > 6) have occurred repeatedly for 0.8 Ma. The total volume of Akan pyroclastic deposits (APDs) is estimated to be 170 km^3 dense rock equivalent (DRE), and most eruptive groups are smaller than 10 km^3 DRE (Hasegawa and Nakagawa 2016). Among them, the ~ 175 ka eruption was by far the largest, with a volume exceeding 55 km^3 DRE (Hasegawa et al. 2009, 2022).

Currently, the Akan Caldera hosts two active volcanoes: Mt. Meakandake (MA) and Mt. Oakandake (OA) (Fig. 1b). Recently, MA has been more active than OA, with its latest magmatic eruption occurring at approximately 1 ka. Intermittent phreatic eruptions have continued to this day (Minami et al. 2021). In the 2000s, phreatic eruptions occurred in 2006 and 2008 at Ponmachineshiri crater (hereafter *P*-crater) (Japan Meteorological Agency 2013). Seismic swarms and volcanic tremors preceded the eruptive activities by a few months prior to the 2006 and 2008 eruptions (Aoyama and Oshima 2015; Ogiso and Yomogida 2021). Additionally, geothermal anomalies with hot springs emerged at the base of MA (Shinohara et al. 2011; Takahashi et al. 2023). In contrast, OA ceased summit eruptions approximately 1000 years ago, and only weak fumarolic and geothermal activity has persisted on its northern flank since then (Tamada and Nakagawa 2009).

Several volcanic unrest episodes without eruptions have been observed around MA and OA. From December 2015 to August 2016, the number of deep low-frequency earthquakes (DLFEs) at depths of 15–25 km increased (Kurihara and Obara 2021). Ground inflation around ~ 5 cm was also detected by Global Navigation Satellite System and Interferometric Synthetic Aperture Radar at the northeastern foot of MA from December 2016 to 2017 (Geospatial Information Authority of Japan 2018). This inflation was modeled as a sill-like pressure source at a depth of approximately 6 km between MA and OA (Fig. 1b, c). Additionally, localized inflation sources (sill and dyke) at a depth of approximately 0.3 km were located on the OA (Fig. 1b, c).

Given the history of large eruptions (> 10 km^3 DRE, VEI > 6) at the Akan Caldera and the recent phreatic eruptions and unrest at the post-caldera volcanoes, evaluating whether such activities could lead to future large eruptions is essential. Specifically, it is essential to evaluate whether a large volume of eruptible magma

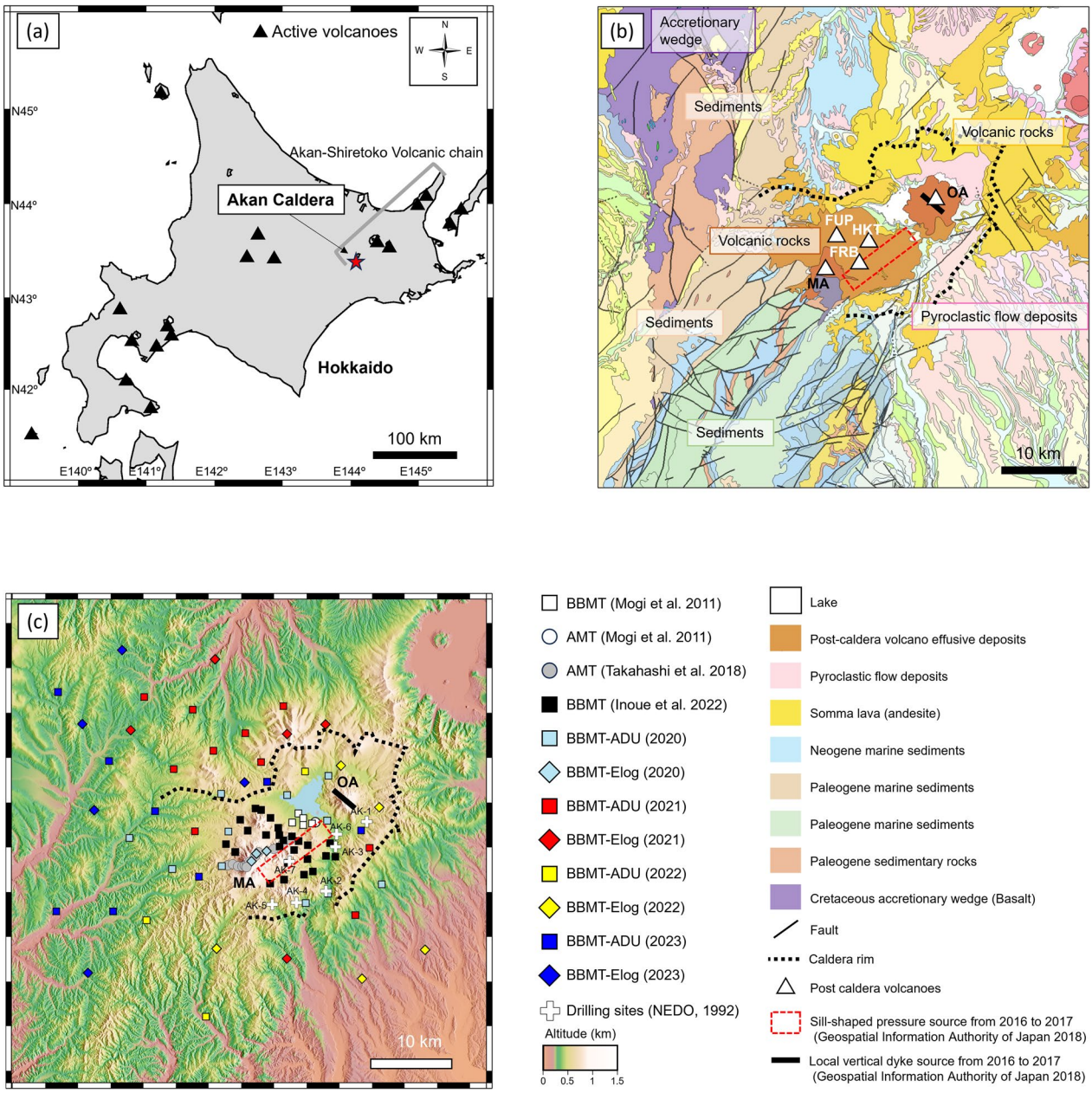


Fig. 1 **a** Location of Akan Caldera in Hokkaido, Japan. Red star indicates the Akan Caldera (study area), and Black triangles indicate active volcanoes. **b** Geological map of the Akan Caldera. The figure is made by a seamless digital geological map of Japan V2 1:200,000 (Geological Survey of Japan, https://gbank.gsj.jp/seamless/v2/viewer/ (in Japanese, accessed on 10 February 2026)). White areas show lakes. The dotted line indicates the caldera rim. Triangles indicate the volcanic cones. MA: Mt. Meakandake. HKT: Mt. Hakuto. FRB: Mt. Furebetsudake. FUP: Fuppushidake. OA: Mt. Oakandake. **c** Location of magnetotelluric sites and topographic map around the Akan Caldera

is currently stored beneath the caldera and whether the recent unrests are related to magma movement. To address these issues, the location, depth, geometry of magma reservoirs, and structure of the magma plumbing system must be known. Such knowledge is critical not only evaluating the potential for future large eruptions but also for understanding the mechanisms behind recent phreatic eruptions and volcanic unrests.

Magnetotelluric (MT) surveys are a powerful tool for imaging the volcanoes' subsurface structure. Since hydrothermal fluids and partial melts are electrically conductive (Gaillard and Maziano 2005; Guo et al. 2017;

Watanabe et al. 2022), MT surveys have been widely used to investigate hydrothermal and magma plumbing systems beneath active volcanoes (Bedrosian et al. 2018; Cordell et al. 2020; Matsushima et al. 2020; Bowles–Martinz and Schultz 2020; Aizawa et al. 2022a; Triahadini et al. 2023; Di Giuseppe et al. 2023). Broadband MT (BBMT) surveys are particularly advantageous because they can resolve resistivity structures at depths ranging from several tens of meters to several tens of kilometers. BBMT has also been applied to various caldera volcanoes (Kelbert et al. 2012; Ichihara et al. 2013; Ogawa et al. 2014; Peacock et al. 2016; Hata et al. 2018; Bertrand et al. 2022; Komori et al. 2024; Iasia et al. 2025). Column-shaped conductive zones have been imaged in the crust of some of these volcanoes and interpreted as magma reservoirs or pathways for magmatic fluids.

To improve volcanic activity evaluation, previous MT surveys have been conducted around MA (Takahashi et al. 2018; Inoue et al. 2022). For example, Takahashi et al. (2018) conducted audio-frequency MT (AMT) surveys in the summit area and obtained a two-dimensional (2D) shallow (< 2 km depth) resistivity model. They interpreted the conductive layers beneath the *P*-crater and Nakamachineshiri crater (hereafter *N*-crater) as fluid reservoirs and clay alteration layers, respectively. Inoue et al. (2022) conducted BBMT surveys around MA and revealed a three-dimensional (3D) resistivity structure extending to several kilometers deep. They identified a conductive column beneath MA; however, they did not investigate the broader magma plumbing system of the volcano or caldera, as their observation was limited to the vicinity of MA. Additionally, no MT sites were directly located on the summit area of MA, leaving the resistivity structure at the top of the conductive column poorly constrained.

In this study, we present a high-resolution image of the subsurface resistivity structure beneath the Akan Caldera, derived from new BBMT surveys combined with data from previous MT studies. Based on this resistivity model and its spatial correlation with observed volcanic activity, we discuss the magma reservoir and associated magma plumbing system beneath the caldera. We also explore the relationship between the shallow hydrothermal system beneath MA and the deeper magma plumbing system of the caldera. The eruption potential of the Akan Caldera was also discussed by integrating our geophysical findings with results from previous petrological studies.

2 Observation method and results

2.1 Magnetotellurics

The MT method is a geophysical technique that utilizes natural electromagnetic (EM) fields to investigate subsurface electrical resistivity structures. The frequency response of EM field variations observed at the Earth's surface is first calculated. These variations are caused by EM induction within the Earth, which is generated by fluctuations in the external EM field.

The MT response—specifically the amplitude and phase—reflects the subsurface resistivity distribution. The relationship between the horizontal electric field (**E**) and the horizontal magnetic field (**H**) observed at the surface is expressed by the impedance tensor (**Z**) as follows:

$$\begin{pmatrix} E_x \\ E_y \end{pmatrix} = \begin{pmatrix} Z_{xx} & Z_{xy} \\ Z_{yx} & Z_{yy} \end{pmatrix} \begin{pmatrix} H_x \\ H_y \end{pmatrix}. \tag{1}$$

The amplitude of each element of $\boldsymbol{Z}$ is associated with the apparent resistivity (ρ), which represents the average resistivity at the depth corresponding to a given EM wave penetration. The apparent resistivity is expressed as follows:

$$\rho_{ij} = \frac{|Z_{ij}|^2}{2\pi f \mu_0}, \tag{2}$$

where f denotes the frequency, and μ_0 denotes the magnetic permeability of free space.

The impedance phase (ϕ) represents the phase difference between the electric and magnetic field components. It is defined for each tensor element as follows:

$$\phi_{ij} = \tan^{-1}\left(\frac{Im(Z_{ij})}{Re(Z_{ij})}\right). \tag{3}$$

This phase is particularly sensitive to the vertical gradient of the subsurface resistivity structure. Another useful MT response is the geomagnetic transfer function ($\boldsymbol{T}$), which relates the vertical magnetic field component to the horizontal components. It is expressed in matrix form as follows:

$$H_z = \begin{pmatrix} T_x \\ T_y \end{pmatrix} \begin{pmatrix} H_x & H_y \end{pmatrix}. \tag{4}$$

The geomagnetic transfer function is often visualized as an induction vector, which is used to assess lateral variations in the resistivity structure.

2.2 Observation and data

We conducted the BBMT survey campaign at 54 sites, covering the whole of the Akan Caldera from 2020 to 2023 (Figs. 1c and S1). We recorded time-series data consisting of two horizontal electric and three magnetic field components at 36 measurement sites using the ADU system (Metronix Geophysics). At 18 sites, we measured two horizontal electric fields by the ELOG system

(NT system design Co. Ltd.) without magnetic components. We used Pb–$PbCl_2$ electrodes and induction coils and occupied each site for approximately 3–10 days. In this study, both the ADU and ELOG systems acquired time series data at a sampling rate of 32 Hz. High-frequency bandwidth data were acquired at sampling rate of 1024 Hz during 1 h at night (UT: 16:00–17:00), when the artificial noise was relatively low.

We calculated the MT responses (impedance tensor and geomagnetic transfer function from approximately 300 to 0.0001 Hz band) from the time-series data using the robust estimation code (BIRRP code; Chave and Thomson 2004). For sites with the ELOG system, we calculated impedance tensors using the magnetic field data of nearby sites measured simultaneously by the ADU system. The MT data were recorded in a geomagnetic coordinate system, whereas the model is defined in geographic coordinates. The geomagnetic declination in Hokkaido (approximately 9°) was accounted for by applying a declination correction during the calculation of the impedance tensor and tipper. We applied the remote reference method (Gamble et al. 1979) to reduce noise using two horizontal magnetic fields measured in Yamagata prefecture (approximately 600 km southwest of the Akan Caldera). We also down-sampled the 32 Hz sampling data to 1 Hz to analyze the long-period bands.

In this study, we incorporated previous BBMT and AMT data collected around MA (Mogi et al. 2011; Takahashi et al. 2018; Inoue et al. 2022). A total of 98 MT sites, comprising 54 newly acquired sites and 44 sites from previous studies, were used. Figure S1 shows the locations of the new and existing MT sites.

To examine the overall characteristics of the dataset, we calculated the induction vectors (Parkinson 1962) and phase tensors (Caldwell et al. 2004), which are robust against galvanic distortion caused by near-surface heterogeneities (Fig. 2).

The phase tensor is defined as $\mathbf{\Phi}=\mathbf{X}^{-1}\mathbf{Y}$, where $\mathbf{X}$ and $\mathbf{Y}$ represent the real and imaginary parts of the complex impedance tensor $\mathbf{Z}$, respectively. The phase tensor $\mathbf{\Phi}$ can be graphically represented as an ellipse whose major and minor axes (Φ_{max} and Φ_{min}) indicate the orientation of the lateral conductivity gradient (Caldwell et al. 2004). For 1D structures, $\Phi_{max} = \Phi_{min}$, while a separation between Φ_{max} and Φ_{min} suggests 2D or 3D structure. Figure 2 shows the rotation invariant $\Phi_2\left(=\sqrt{\Phi_{xx}\Phi_{yy}-\Phi_{xy}\Phi_{yx}}=\sqrt{\Phi_{max}\Phi_{min}}\right)$ by the ellipse color. This parameter indicates the vertical conductivity gradient.

Overall, at a short period (0.25 s), the phase tensor ellipses exhibit a circular shape, whereas at longer periods, they become elongated in an E–W to ESE–WNW direction. At most sites, Φ_2 exceeds 45° at 0.25 s, indicating a decrease in resistivity with depth at shallow levels beneath the Akan Caldera.

The induction vectors at periods longer than 50 s show a contrasting pattern around MA. In the western and eastern regions, the vectors point eastward and southwestward, respectively (Fig. 2), suggesting a significant difference in the resistivity structure between the eastern and western parts of MA.

At some sites in the western part of MA (e.g., M45, T10, Z190; see Fig. S2), the Z_{yx} component shows phases out of the quadrant range (−180° and −90°) in the long-period band (approximately 500–3000 s). Such MT impedance phases that exceed ± 90° in the off-diagonal components are referred to as anomalous phases or phase out-of-quadrant (POQ), and have been reported in various other volcanic and tectonic settings (Jones et al. 1988; Heise and Pous 2003; Ichihara et al. 2013, 2019; Aizawa et al. 2014, 2022a; Raju et al. 2022).

Previous studies have demonstrated that strong 3D resistivity contrasts and strong deflection of currents in the subsurface can produce POQ responses, as shown through 3D geometries (Egbert 1990; Weckmann et al. 2003; Ichihara and Mogi 2009; Piña-Varas and Dentith 2018; Raju and Patro 2023; Inoue and Hashimoto 2024). In this study, we estimate the resistivity structure that reproduces the observed POQ features using 3D inversion and discuss their origin in the next section (Sect. 3).

3 Three-dimensional inversion analysis

3.1 Inversion modeling

The 3D resistivity structure was estimated through inverse modeling of MT data at all 98 sites using FEMTIC code (Usui 2015; Usui et al. 2017, 2024). FEMTIC employs finite element meshes, which allow for a more accurate representation of smooth terrain. In contrast, Inoue et al. (2022) used a stair-step mesh to model the topography. To obtain a resistivity structure that best explains the observed MT transfer functions, FEMTIC minimizes the following objective function:

$$\phi\left(\mathbf{m_p}\right)=\phi_{\mathrm{d}}\left(\mathbf{m_p}\right)+\alpha^2\phi_{\mathrm{m}}\left(\mathbf{m_p}\right) \tag{5}$$

where $\mathbf{m_p}$ denotes the vector of model parameters representing the resistivity at all mesh elements. The first and second terms on the right-hand side represent data misfit and model roughness, respectively. The hyperparameter α controls the tradeoff between data fitting and maintaining a smooth resistivity model.

Figure 3 shows the computational mesh used in this study. We set the positive X direction to the geodetic north. Using the deformed hexahedral elements, the topography and land-sea distribution were incorporated into the computational mesh. The model domain

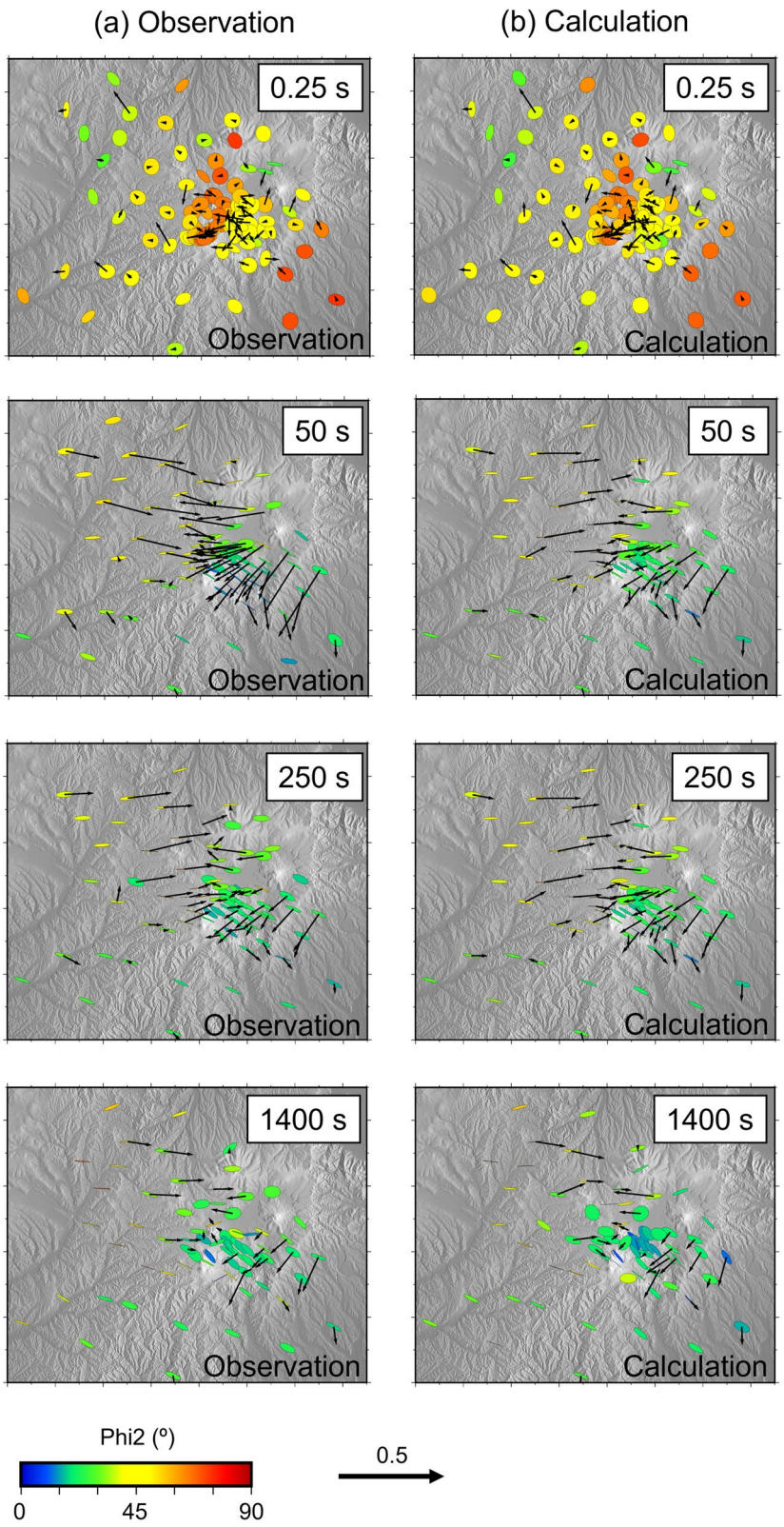


Fig. 2 Comparison between observations (left) and responses calculated (right) by the phase tensors and the real induction vectors (Parkinson convention) at the three selected periods. Each ellipse is normalized by its major-axis length and filled with a color indicating the magnitude of arctan (Φ_2)

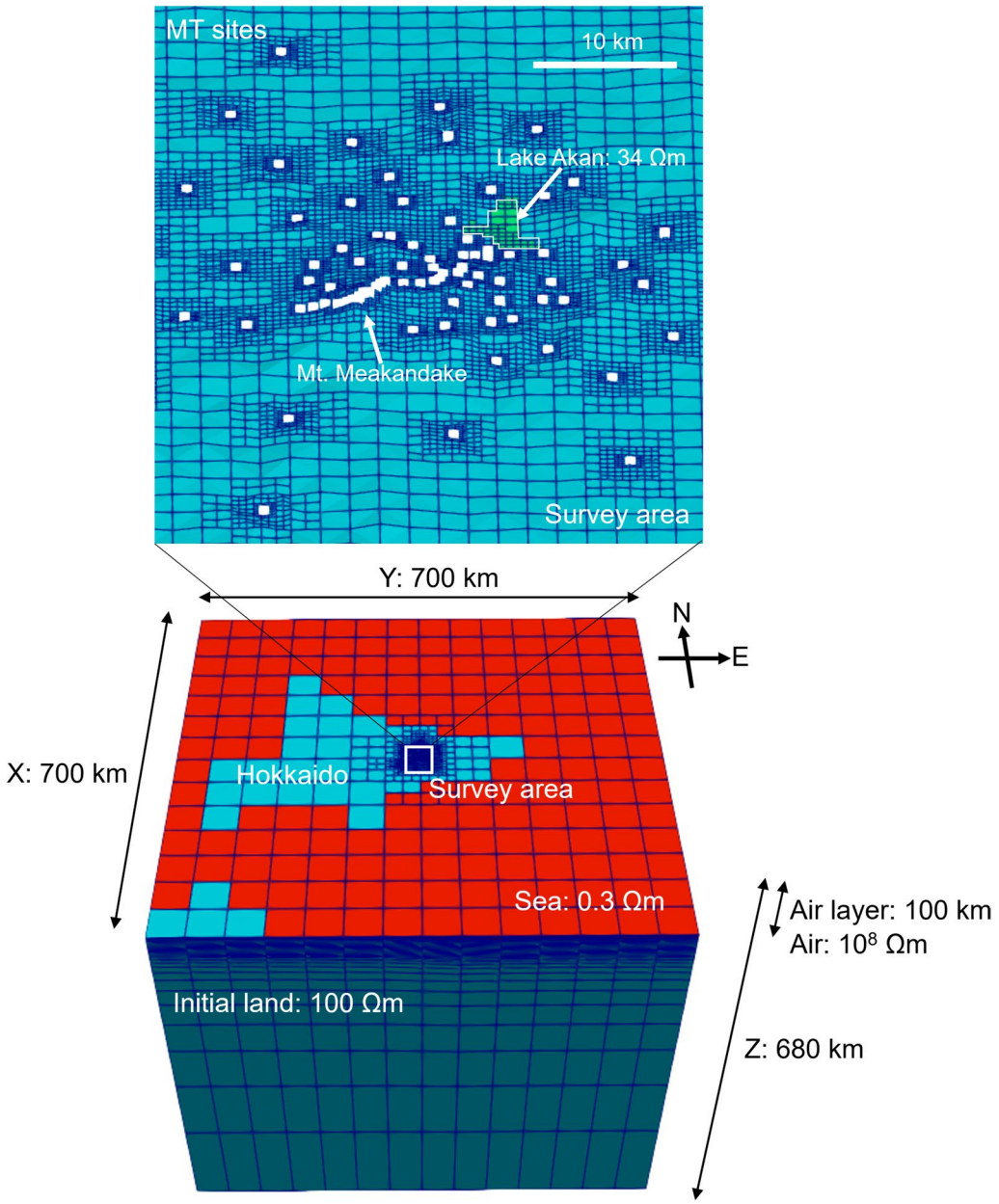


Fig. 3 Computational mesh used for 3D resistivity inversion. Each element is colored according to the initial model resistivity. The air layer is omitted for clarity. The number of land elements is 216,523. Upper part: detailed view of the survey area; a finer mesh is used around the MT observation sites. Lower part: overall view of the calculation area

extends 700 km in the X direction, 700 km in the Y direction, and 680 km in the Z direction. The uppermost 100 km of the model is treated as air layers, composed of vertically stacked meshes with thicknesses of 250 m × 2, 500 m × 2, 1 km × 2, 2 km × 3, 5 km × 4, 10 km × 2, followed by 20 km and 30 km layers upward) from the surface (Fig. 3). First, we divided the vertical direction into a mesh of 25 m intervals from the surface to 200 m (surface $< Z <$ 0.2 km) and increased the mesh by a factor of 1.4 from 200 to 500 m until the layer thickness exceeded 100 m (0.2 $< Z <$ 0.5 km). Subsequently, a layer thickness of 0.13 km was set for the range up to $Z = 2$ km (0.5 $< Z <$ 2 km). From $Z = 2$ km to $Z = 8.5$ km, we also increased the layer thickness by a factor of 1.4 until it reached approximately 2 km, and from $Z = 8.5$ km to $Z = 39$ km, we divided it in meshes of every 2 km. At subsequent depths, the layer thickness was also increased by a factor of 1.4. Second,

the horizontal length in the computational mesh was divided by 50 km square elements. Near the MT sites, the mesh was locally refined with element sizes of 200 m within a 1 km × 1 km area, and 500 m within a 2.5 km × 2.5 km area.

To include topography and bathymetry into the mesh, we used the 10-m-mesh data of the Geospatial Information Authority of Japan and the 500-m-mesh digital elevation model around Japan [J-EGG500: https://www.jodc.go.jp/vpage/depth500_file.html (accessed on 23 November 2025)] for calculation areas (Fig. 3). A uniform initial resistivity of 100 Ωm was assigned to the solid Earth, while the resistivities of the sea and air were fixed at 0.3 and 10^8 Ωm, respectively. Lake Akan was included in the model, and its resistivity was fixed at 34 Ωm according to the value measured by Wakana et al. (2023).

The full components of the impedance tensor (real and imaginary parts of Z_{ij}) and the geomagnetic transfer function (real and imaginary parts of T_{ij}) were used as the input data for inversion. Before the inversion, we removed the apparent outliers in the sounding curves. We selected 9–17 frequencies ranging from 5200 to 1 Hz at each AMT site, and from 320 to 0.00034 Hz at each BBMT site. The error floors of the impedance tensor and the geomagnetic transfer function were set to 5% (off-diagonal components) and 10% (diagonal components) of $\sqrt{|Z_{xy}| \cdot |Z_{yx}|}$ and 0.02, respectively.

In this modeling, we examined several different α ($\alpha = 0.3, 1, 2, 4, 7, 10, 30, 100$) to select the preferred model using the L-curve criteria (Yoshimura et al. 2018; Usui et al. 2024). Figure 4 shows the L-curve of the data misfit and model roughness for the respective α values. As shown in the figure, the points corresponding to $\alpha = 2$ and $\alpha = 4$ appear to be the "knee" of the curve. The data fitness showed that the model with $\alpha = 2$ reproduced the observation values better than the model with $\alpha = 4$. We found that the model with $\alpha = 2$ reproduced the phase curves well, including the POQ features. Therefore, we selected the model with $\alpha = 2$ as the optimal inversion result. We also tested an inversion with $\beta = 0.01$, where β is a hyperparameter that penalizes the galvanic distortion term (Usui 2015). In this study, we adopted the inversion using only α, as it provided better agreement between the 3D resistivity structure and the electrical logging data reported by New Energy and Industrial Technology Development Organization (NEDO) (1992).

The inversion process was terminated when the objective function was decreased by 1% when compared with the previous iteration. As a result, the root-mean-square (RMS) misfit improved from 14.48 (initial model) to 2.19 (final model at iteration 10). Figure 2 shows the fitting results for the induction vectors and phase tensors. Overall, the final resistivity model well explained the observed induction vectors and phase tensors. The POQ data observed in the Z_{yx} components were also successfully reproduced by the final model (Fig. S2). We evaluated the data fit at all sites and confirmed that the final model successfully explained the observed MT responses (Figs. 2 and S2).

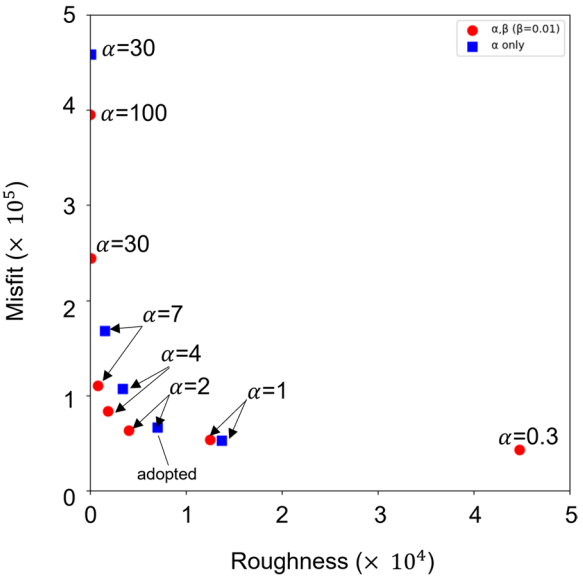


Fig. 4 L-curve obtained from the 3D inversion results with various trade-off parameter patterns. The horizontal and vertical axes represent the model roughness and data misfit of the objective function, resistivity. This study adopted $\alpha = 2$

3.2 Inversion results

Figures 5 and 6 show the horizontal and vertical slices of the optimal resistivity model, respectively. The most prominent feature is a conductive anomaly (C1) located at the center of the Akan Caldera, with its root deepening westward. From the vertical slices (Fig. 6), this conductive anomaly can be subdivided into three zones by depth. At depths of approximately 0.5–3 km, the conductive anomaly C1a (resistivity ~ 1–10 Ωm) lies directly beneath MA. Between 3 and 15 km depth, the conductive anomaly C1b appears beneath the central part of the caldera. At depths greater than 15 km, the conductive anomaly C1c extends beneath the western part of the caldera. These three anomalies connect to form a single conductive column with a resistivity of approximately 10 Ωm.

The C1 anomaly imaged in this study is significantly larger than that identified by Inoue et al. (2022). Inoue et al. (2022) used the ModEM code (Egbert and Kelbert 2012; Kelbert et al. 2014), which employs a

finite-difference method. They considered fewer sites (38 sites in Inoue et al (2022), while 98 sites in this study) with an observation area limited to the vicinity of MA. In contrast, our dataset covers a wider area and incorporates previous MT data (Takahashi et al. 2018) near the MA summit, where Inoue et al. (2022) did not conduct observations. Thanks to the addition of these MT sites, our survey fully covers the low-resistivity anomaly C1, enabling the first detailed imaging of its entire structure.

Outside the Akan Caldera, two distinct conductive layers (C2 and C3) were observed at relatively shallow depths (Fig. 5; depths of 0.5 and 1.5 km). With increasing depth, C2 extends southeastward, whereas C3 extends northwestward. We also imaged a surface conductive layer near the MA summit area, hereafter referred to as conductive anomaly of MA (CM). CM is located between the summit and the northeastern foot of MA (Fig. 6). The model suggests that CM and C1 have spatially distinct features, with CM having a thickness of approximately 1–2 km.

Several characteristic high-resistivity anomalies are distributed near the Akan Caldera. The high-resistivity body R1 extends from the surface to a depth of approximately 3 km along the northeastern foot of MA. Additionally, two high-resistivity bodies, RW and RE, are present. The RE extends from a depth of approximately 1 km to greater depths, following the eastern caldera rim.

3.3 Sensitivity tests

We performed sensitivity tests to constrain the possible range of resistivity values for C1a, C1b, CM and C1c using the following approach. In each part, conductive anomalies were defined as regions with resistivity values below 30 Ωm. We then varied the resistivity values of these anomalies in each region and performed forward modeling to calculate the impedance and geomagnetic transfer functions. Finally, we computed the RMS misfit between the calculated and observed values.

Figure 7 shows the variation in RMS misfit as the resistivity of blocks with values below 30 Ωm was systematically varied from 0.1 to 30 Ωm. For each region, the RMS misfit, approaches that of the optimal model when a bulk resistivity of a few Ωm (Fig. 7). The upper region (C1a, C1b and CM) exhibits a sharp increase in RMS misfit at resistivity values outside the range of 3–10 Ωm. In this study, resistivity values are considered unreasonable when RMS misfit increases to 2.29 or higher, when compared with 2.19 for the optimal model. Based on the results shown in Fig. 7, the inferred resistivity ranges are approximately 3–10 Ωm for C1a, 5–10 Ωm for C1b, and 3–10 Ωm for CM. In contrast, the lower region (C1c) does not show an RMS misfit exceeding 2.29 within the tested range of 0.1–30 Ωm. A broader sensitivity test, extending from 0.01 to 1000 Ωm for blocks surrounding C1c (Fig. S4), indicates that the plausible resistivity range of C1c is approximately less than 70 Ωm.

We also consider two additional anomalies examined through sensitivity tests: the conductive layer CM beneath the MA summit area and the conductive body C4 located on the northern side of the Akan Caldera. Figure 7 shows that the CM is robust and is located directly above C1. C4, which was identified as a large-scale conductive anomaly located outside the survey area, exhibited relatively minor changes. Based on the result and the fact that C4 lies beyond the area covered by MT sites, we conclude that C4 is not sufficiently constrained.

3.4 Relationship between POQ and the shape of conductive column

In our MT survey, POQ features were widely observed on the western side of the Akan Caldera, suggesting a relationship with the geometry of C1. Figure S5 shows the distribution of MT sites, where POQ appeared in the Z_{yx} component, both in the observed data and inversion results. In some cases, POQ was interpreted as an obliquely inclined conductive column (Lindsey et al. 2016; Inoue and Hashimoto 2024). By comparing the distribution of the POQ data with the geometry of C1b, we concluded that the POQ in the Z_{yx} component is caused by a westward-inclined conductive column, which is consistent with the model proposed by Inoue and Hashimoto (2024). Inoue and Hashimoto (2024) demonstrated that current channeling occurs when a conductive column is inclined, resulting in the electric field being drawn into the conductor.

We emphasize that the occurrence of POQ is closely related to the geometry of C1. To demonstrate this relationship, we conducted synthetic tests in which the depth to the base of C1 10 Ωm) was systematically modified by truncating its lower boundary (Fig. S6). Complete

(See figure on next page.)

Fig. 5 Map view of the estimated electrical resistivity structure. Small black squares and circles indicate BBMT and AMT sites, respectively. White circles indicate the hypocenters of regular earthquakes (2004–March 2023), determined by the Japan Meteorological Agency. Hypocenters located within ± 0.5 km of the respective depth are shown. Red circles indicate the deep low-frequency earthquakes (Kurihara and Obara 2021). Black line indicates the topography contour (> 0.45 km above sea level). White line indicates the Akan Caldera rim. White triangles shown in the slices at the depths of 10, 15, and 20 km indicate MA (Mt. Meakandake) and OA (Mt. Oakandake)

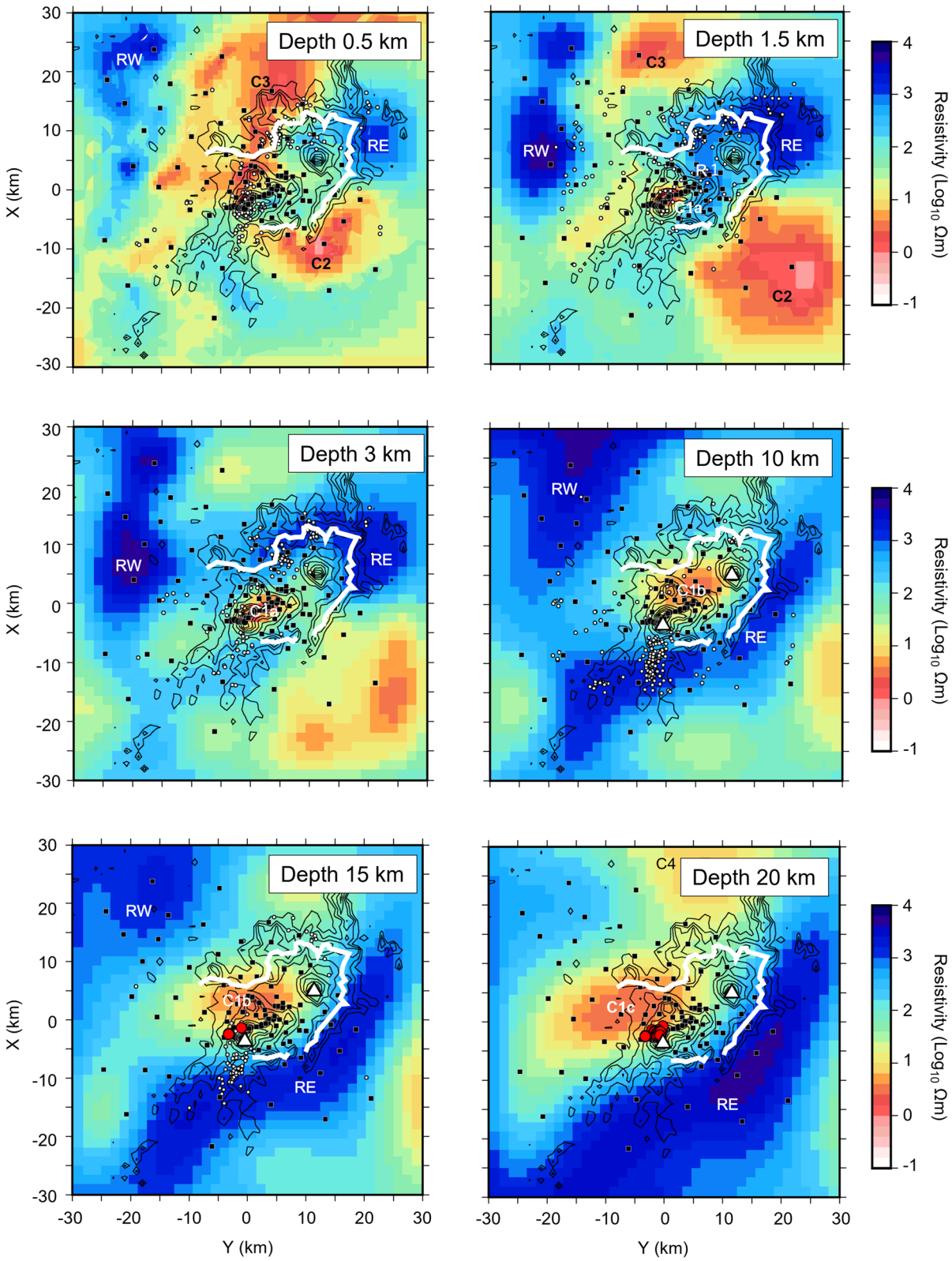


Fig. 5 (See legend on previous page.)

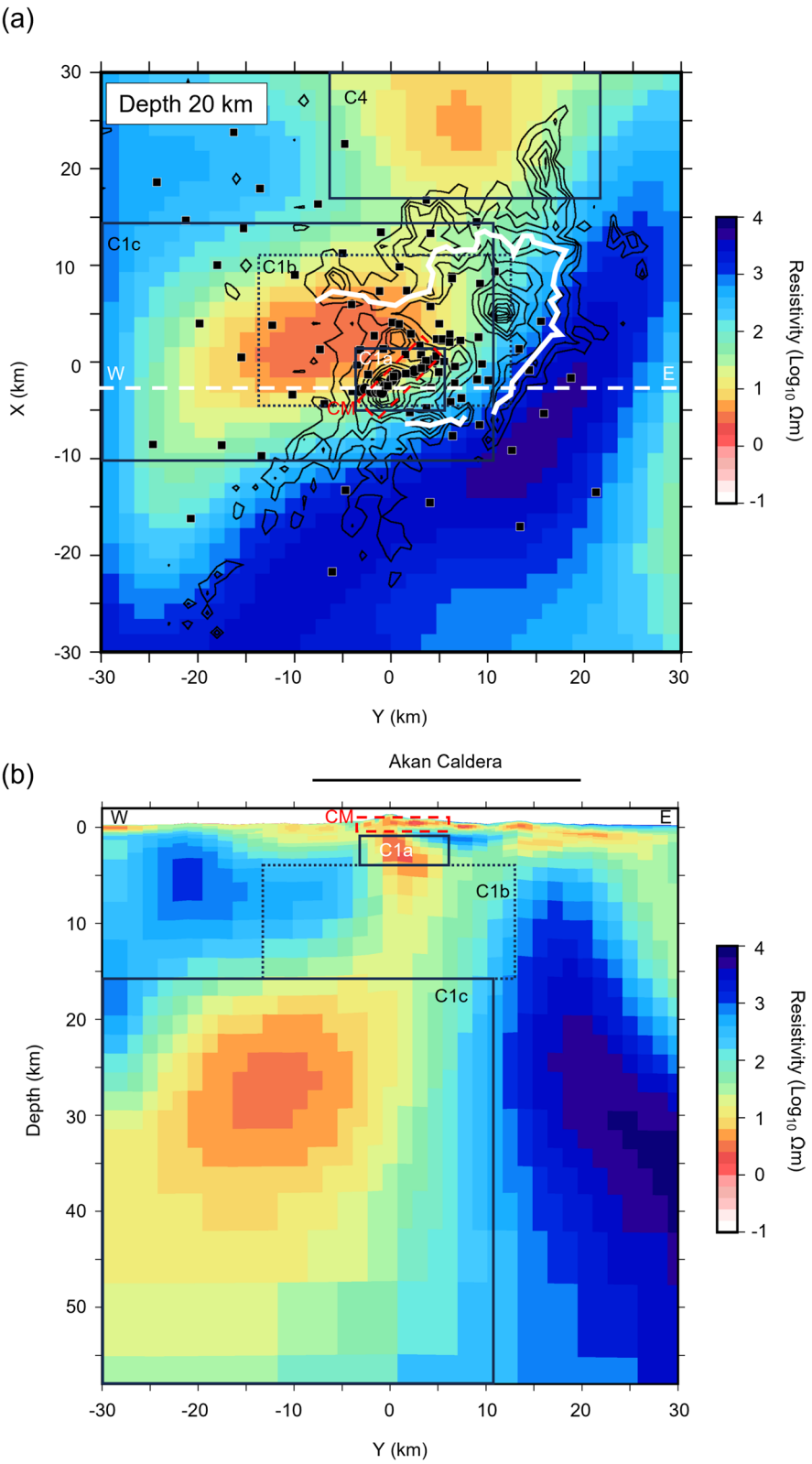


Fig. 6 Area where the sensitivity test was performed. **a** Horizontal section of the final model. The dots indicate the location of MT sites. **b** E–W vertical section of the final model along the white dot line shown in (**a**). Modified models were created by changing the resistivity values of the elements within the rectangular region whose resistivity is lower than 30 Ωm

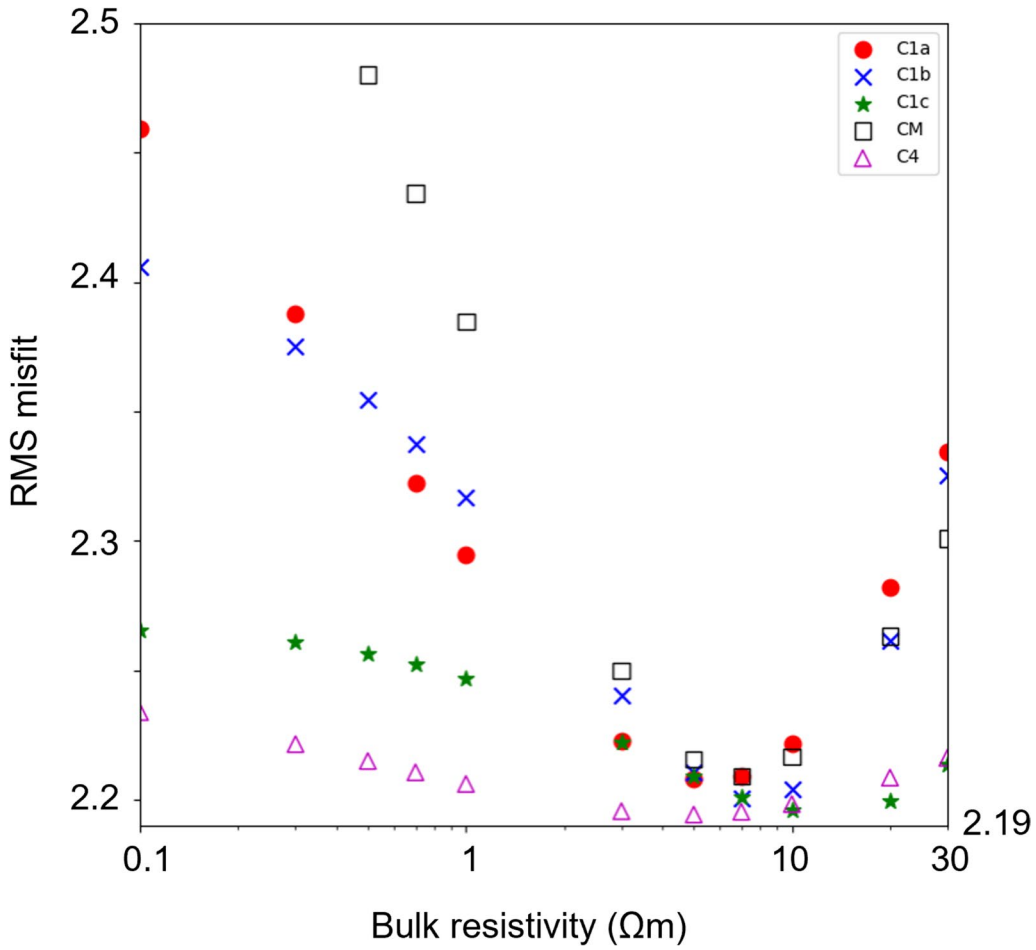


Fig. 7 Sensitivity test for the resistivity values of three parts of the conductive body C1, C4, and CM (refer to Fig. 6). We modified the conductive anomaly as those with 30 Ωm or less and replaced the bulk resistivity accordingly

removal of C1 fails to reproduce the POQ. Reducing the base of C1 from ~ 30 km to 10 km significantly alters the synthetic sounding curves and results in a mismatch with the observed POQ. These results indicate that the vertical extent of C1 extent strong control on the manifestation of POQ. We further investigated the effect of near-surface resistivity on the POQ by replacing all resistivity values from the C3 with a uniform value of 100 Ωm. The POQ remained substantially unchanged under this modification (Fig. S7), indicating that C1 is the primary contributor to the POQ in this region. Collectively, these results provide additional support for the interpretation proposed by Inoue and Hashimoto (2024).

4 Discussion

4.1 Interpretation of the resistivity structure

4.1.1 Central part of the Akan Caldera (C1b)

C1b, with resistivity values ranging from 5 to 10 Ωm, is the conductive anomaly located at depths of approximately 3–15 km (Figs. 6 and 8). Its horizontal extent covers a wide area within the Akan Caldera (Figs. 5 and 8). The estimated volume of C1b (the elliptical cylinder) is greater than approximately 500 km^3. When compared with seismic activity, the hypocenters were distributed around C1b (Figs. 5 and S5). We interpret that C1b partly serves as a possible pathway for magmatic fluids rising from deeper sources toward MA, and potentially also toward Mt. Oakandake (OA). The hypocenters of DLFEs recorded during the swarm period from 2015 to 2016—identified using the matched filter technique (Kurihara and Obara 2021)—and a sill-shaped pressure source estimated during the 2016–2017 unrest (Geospatial Information Authority of Japan 2018) are located at the bottom and top of C1b, respectively (Fig. 8). Notably, the sill-shaped pressure source was activated approximately 1 year after the deep cluster of the DLFEs increased. This time lag suggests that fluid upwelling along C1b may be slow on the order of ~ 0.05 km/day, as compared to other active volcanoes and events (e.g. Fig. 7 in Kurihara and Obara (2021)).

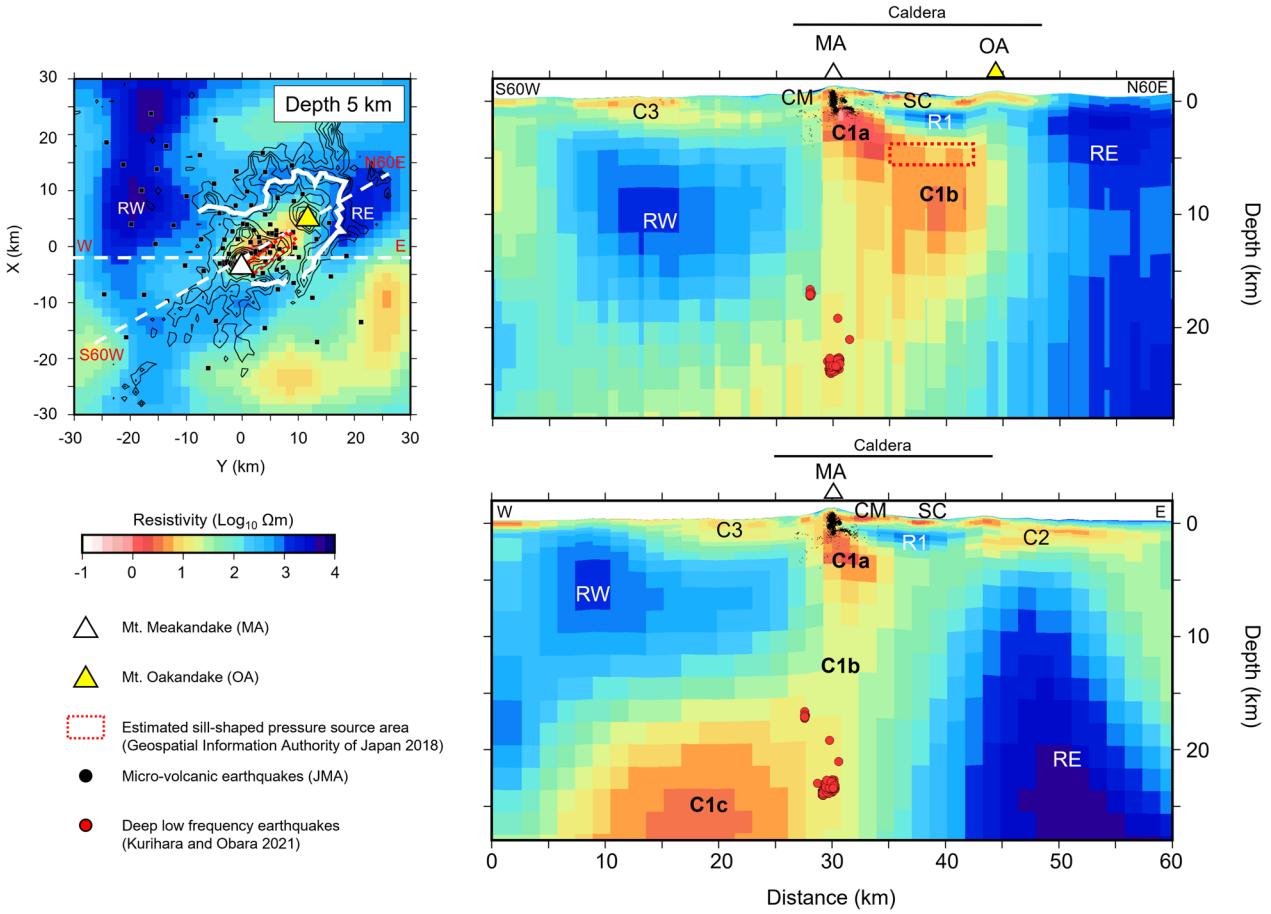


Fig. 8 Left column: horizontal slices. Right column: vertical slice along lines E–W and NE–SW shown by the white dotted lines in horizontal slices. Red circles indicate the hypocenters of deep low-frequency earthquakes, determined by Kurihara and Obara (2021). Black circles indicate the hypocenters of volcanic earthquakes that occurred between 2004 and 2019 around Mt. Meakandake (provided by Sapporo Regional Headquarters, JMA)

C1b flattens in a northeast–southwest direction at depths of approximately 3–5 km (Fig. 8), directly above the sill-shaped pressure source. This orientation aligns with the major axis of the caldera shape. It is worth noting that the active volcanoes of MA and OA are located near the southwestern and northeastern edges of C1b, respectively (Figs. 5 and 8). Considering that the lateral extent of C1b and the distribution of post-caldera volcanoes, we believe that C1b is a key structure for understanding volcanic activity in the caldera.

Conductive columns, including caldera systems, are often imaged beneath active volcanoes. Typically, such features appear as inclined "columns" (e.g. Ogawa et al. 2014; Hata et al. 2018; Matsushima et al. 2020; Aizawa et al. 2025), whereas C1b is significantly broader than these examples. We speculate that C1b represents a large, mushy magma reservoir that is primarily immobile and non-eruptible. In contrast, mobile and eruptible magma or magmatic fluid may ascend from the zone of DLFEs and the deeper part of C1c. The magma plumbing system of the Akan Caldera is discussed in detail in Sect. 4.2.

The magma composition of MA ranges from rhyolitic to basaltic (Wada et al. 1998). The rhyolitic (Guo et al. 2016), dacitic (Laumonier et al. 2015), and basaltic (Scarlato et al. 2004) melt resistivities were assumed based on the temperature and pressure conditions of primary melts reported by Wada (1991) and Kuritani et al. (2021). We calculated the relationship between melt fraction and bulk resistivity based on the formulation by Hashin and Shtrikman (1962) (Fig. S8). Based on comparison with the sensitivity tests (Sect. 3.3), C1b is estimated to have a melt fraction of approximately 20–25% or 10–20% if the melt is dacitic or rhyolitic, respectively. The estimated melt fractions correspond to crystal mush (Bachmann and Bergantz 2008). C1b may largely represent a non-eruptible magma reservoir, and magma supply from deeper levels could be a key factor in the eruption process. We speculate that a small amount of

eruptible magma surrounded by crystal mush exists in C1b. Indeed, Cashman et al. (2017) proposed that such systems consist of multiple melt lenses partially connected by vertical conduits surrounded by a volumetrically dominant crystal mush.

4.1.2 Deep and western part of the Akan Caldera (C1c)

At depths greater than 15 km, the conductive anomaly C1c extends beneath the western part of the Akan Caldera. The estimated volume of C1c is greater than 4500 km^3. The primary magmas of MA were estimated to be in equilibrium at temperatures of 1210–1230 °C and pressures of 0.9–1.0 GPa, corresponding to below Moho (Kuritani et al. 2021). DLFEs beneath MA have been observed at depths of approximately 30 km (Kurihara and Obara 2021). These findings indicate that C1c is a magmatic reservoir fed from mantle depths. Although C1c appears to extend to even greater depths, its lower boundary and the bulk resistivity are not strongly constrained in this study (Figs. 6 and 7).

The spatial relationship between DLFEs and the C1c and C1b conductive anomalies is of particular interest. A vertical slice along the W–E profile across MA (Fig. 8) shows that the DLFEs during the swarm period of 2015–2016 are located near the kink in the conductive structure—at the junction between C1c and C1b—corresponding to the outer edges of both. A similar spatial relationship has been reported at the Kuju Volcano (Aizawa et al. 2022a) and Gassan Volcano (Usui et al. 2024), both in Japan. DLFEs from 2015 to 2016 occurred in nine episodes, recurring approximately every 2 weeks (Kurihara and Obara 2021). Multiple mechanisms have been proposed to explain DLFEs, including the cooling magma, degassing, intermittent magma flow, and second boiling models (Kurihara and Obara 2021). DLFE swarms beneath active volcanoes are generally associated with the ascent of volatile-rich magmas from the mantle (Melnik et al. 2020). Intermittent magma flow caused by the periodic opening of barriers in the conduit has been suggested as a trigger for DLFEs (Ukawa and Ohtake 1987).

Given the spatial relationship between the DLFEs and conductive zones, we suggest that the DLFEs are generated by the ascent of magmatic fluids. Although the exact mechanism remains uncertain, the distribution of DLFE implies that fluid migration occurs along the edges of C1c (Fig. 8).

4.1.3 Shallow part of the post-caldera volcano (C1a and CM)

Figure 9 shows a close-up view of the optimal resistivity model around MA. C1a is located at a depth between 1 and 5 km below sea level (BSL), and its estimated volume is approximately 10 km^3. Micro-earthquakes are concentrated in two columnar clusters located between C1a and CM. The top of C1a corresponds to the base of the seismic clusters. The open crack that explains the ground tilt changes (Aoyama and Ohshima 2015), and the tremor source region identified prior to the 2008 phreatic eruption (Ogiso and Yomogida 2021), are also located between C1a and CM (Fig. 9). These precursory activities are interpreted as resulting from the rapid ascent of hydrothermal fluids. We interpret C1a as a volatile-rich zone that supplied fluids prior to the 2008 phreatic eruption. Within C1a, a mushy magma may coexist with magmatic volatiles. We infer that the proportion of volatiles exsolved from magma is likely higher in the shallow part of C1 (i.e., C1a) owing to their buoyancy. Analyses of volcanic gases from the summit crater area indicate that the N and P craters, which are approximately 1 km apart, share a common magmatic source (Shinohara et al. 2011), suggesting that C1a may represent the source of the volcanic gases. The shallower unit CM is interpreted as a clay-rich layer that partially caps the hydrothermal system, consistent with demagnetization beneath CM that has been interpreted as resulting from temperature increases associated with the accumulation of hydrothermal fluids. Such conductive anomalies, interpreted as hydrothermal reservoirs and cap rocks, have been revealed by resistivity structural studies as zones associated with volcanic eruptions and unrest (Yamaya et al. 2013; Piña Varas et al. 2014; Hogg et al. 2018; Tsukamoto et al. 2018; Kanda et al. 2019; Hashimoto et al. 2020; Tseng et al. 2020; Di Giuseppe et al. 2023). Ascending magmatic fluids influence the shallow hydrothermal system in a volcano, triggering eruptions or unrest (e.g., Ohba et al. 2021; Mannen et al. 2021). The explosive expansion of ground water due to the heat supplied from ascending hydrothermal fluids can trigger phreatic eruptions (Stix and de Moor 2018; Narita et al. 2020; Terada et al. 2021; Aizawa et al. 2022b). Therefore, investigating how fluids are supplied to CM from C1a is essential for understanding the phreatic eruptions of MA.

4.1.4 Shallow conductor outside of the Akan Caldera (C2 and C3)

According to the geological map, the extensive shallow conductive layers closely correspond to sedimentary rock formations. C3 is a conductive layer extending north of the caldera, distributed at depths of approximately 0–2 km. Since C3 mainly corresponds to Neogene marine sediments (Fig. 1b), it represents the sediments distributed to the north of the caldera.

C2 is a conductive layer found at depths of 0–2 km BSL and is widely distributed in the southeastern part of the Akan Caldera. Its extent closely aligns with the distribution of pyroclastic flow deposits from the caldera-forming eruption (Fig. 1b) and areas of low-gravity anomalies

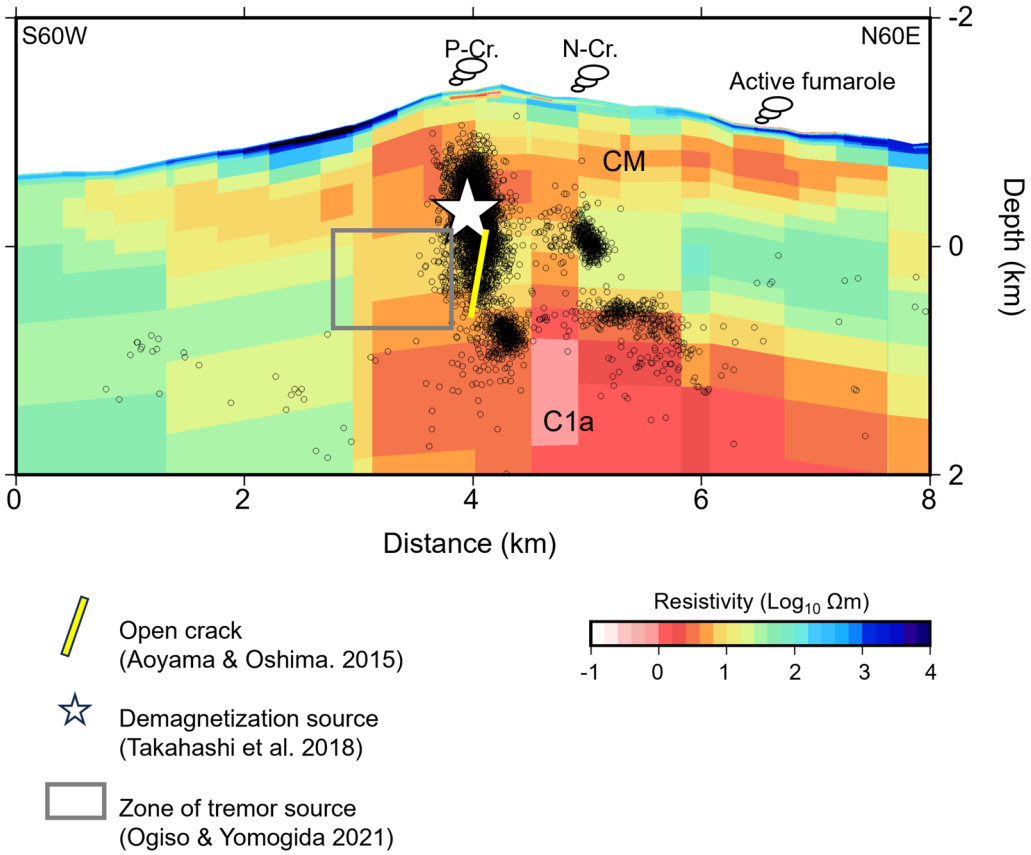


Fig. 9 Vertical section beneath Mt. Meakandake (along with black line in Fig. S9). The star is demagnetization source of the period from before to after the 2008 eruption (Takahashi et al. 2018). The line is the location of the opening dike modeled by Aoyama and Oshima (2015). The rectangle is the zone of volcanic tremor source prior to the 2008 eruption estimated by Ogiso and Yomogida (2021). Black circles indicate the hypocenters of volcanic earthquakes that occurred between 2004 and 2019 around Mt. Meakandake (provided by Sapporo Regional Headquarters, JMA)

(Hasegawa et al. 2009, 2022). C2 is interpreted as a pyroclastic flow deposit originating from the Akan Caldera.

4.1.5 Resistive zones outside the Akan Caldera (RW and RE)

A comparison with the surface geological map reveals that the high-resistivity zone RW (0–15 km BSL), located on the western side of the caldera, corresponds well with the Cretaceous accretionary wedge, which is mainly composed of basalt (Fig. 1b). Geologically older rocks typically exhibit high resistivity due to their low fluid content and complete cooling. In contrast, the high-resistivity zone RE, located along the eastern to southeastern rim of the caldera, is interpreted as andesitic basement rock. This interpretation is supported by Inoue et al. (2022), who based their conclusion on drilling data (NEDO 1992) and a Bouguer gravity anomaly map (Hasegawa et al. 2009). We adopted the same interpretation in this study. The two high-resistivity anomalies extend to depths greater than 20 km. Such deep resistive bodies are sometimes interpreted as plutonic rocks formed by past magmatic activity (Peacock et al. 2015; Bedrosian et al. 2018; Aizawa et al. 2022a). The deeper portions of the high-resistivity anomalies may represent plutonic bodies.

4.1.6 Resistive zone within the caldera (R1)

A high resistivity R1 (Fig. 5, depth 1.5 km), located within the Akan Caldera, may be a part of the andesitic basement segmented during the MA and OA formation. When compared with the drilling data within the Akan Caldera, R1 may represent a dense, high-temperature rock body. The temperature logging data at R1 exhibit conductive temperature profiles (Fig. S3; AK-3,6). AK-3 and AK-6 are consistent with their relatively low porosity and high elastic wave velocity and can be interpreted as dense, high-temperature rock bodies. Situated just above C1b, R1 serves as a barrier to the upward transport of fluids from C1b.

We propose that R1 represents a remnant body of andesitic basement rock left behind during the formation of the two active volcanoes, MA and OA. The cross-section at a depth of 1.5 km (Fig. 5) shows that the areas around MA and OA exhibit relatively low resistivity,

whereas R1 and RE are partially connected. Assuming that the conductive zones represent pathways for fluids and magma, this connectivity may indicate structural disruption during caldera formation.

4.1.7 Surface conductive zone within the caldera (SC)

A near-surface conductive layer (SC) was observed in the geothermal area on the northeastern flank of MA (Figs. 8 and S9). A hydrothermal system was distributed from the eastern to northeastern foot of MA, possibly causing fumarolic activity and hot water pools at the surface (Takahashi et al. 2023). Drilling data indicate relatively high porosity and low elastic velocity in this zone (Fig. S3), suggesting that SC is rich in hydrothermal fluids or groundwater. However, the temperature log at a depth corresponding to SC (AK-7, approximately 0.5 km deep) shows a conductive thermal gradient (Fig. S3), which is inconsistent with the interpretation of a fluid-rich zone. One possible explanation for this apparent contradiction is the presence of clay minerals. Conductive clay minerals, such as smectite, contain bound water and ions that can significantly reduce resistivity, even when present in small amounts. According to NEDO (1992), the rock samples used in laboratory measurements were dried at temperatures exceeding 100 °C before the porosity measurement. This drying process may have caused the evaporation of the clay-bound water, resulting in artificially high porosity measurements as compared to in-situ conditions. Therefore, SC can be interpreted as a clay-rich layer with a conductive thermal profile and low resistivity.

4.2 Magma plumbing system of Akan Caldera

In this section, we discuss the magma plumbing system of the Akan Caldera, including the pathways through which magmatic fluids ascend and are supplied to the caldera. Our interpretation is summarized in Fig. 10. C1b functions as a magma reservoir and a pathway for fluid ascent, playing a key role in the overall magmatic structure of the Akan Caldera. C1c, located at a greater depth, corresponds to a deep-seated magma reservoir that supplies magmatic fluids to C1b.

We propose that C1b and C1c represent a vertically structured magma storage system that may have contributed to the formation of the Akan Caldera and the growth of post-caldera volcanic edifices. We suggest that magmatic fluids are usually supplied to and ascend along the edges of C1b because MA and OA are located above its edge and DLFE occurs there (Fig. 5 and 8). This "edge-ascent" hypothesis—i.e., that magmatic fluids ascend along structural boundaries—has been recently proposed (e.g., Aizawa et al. 2022a, 2026; Triahadini et al. 2023;

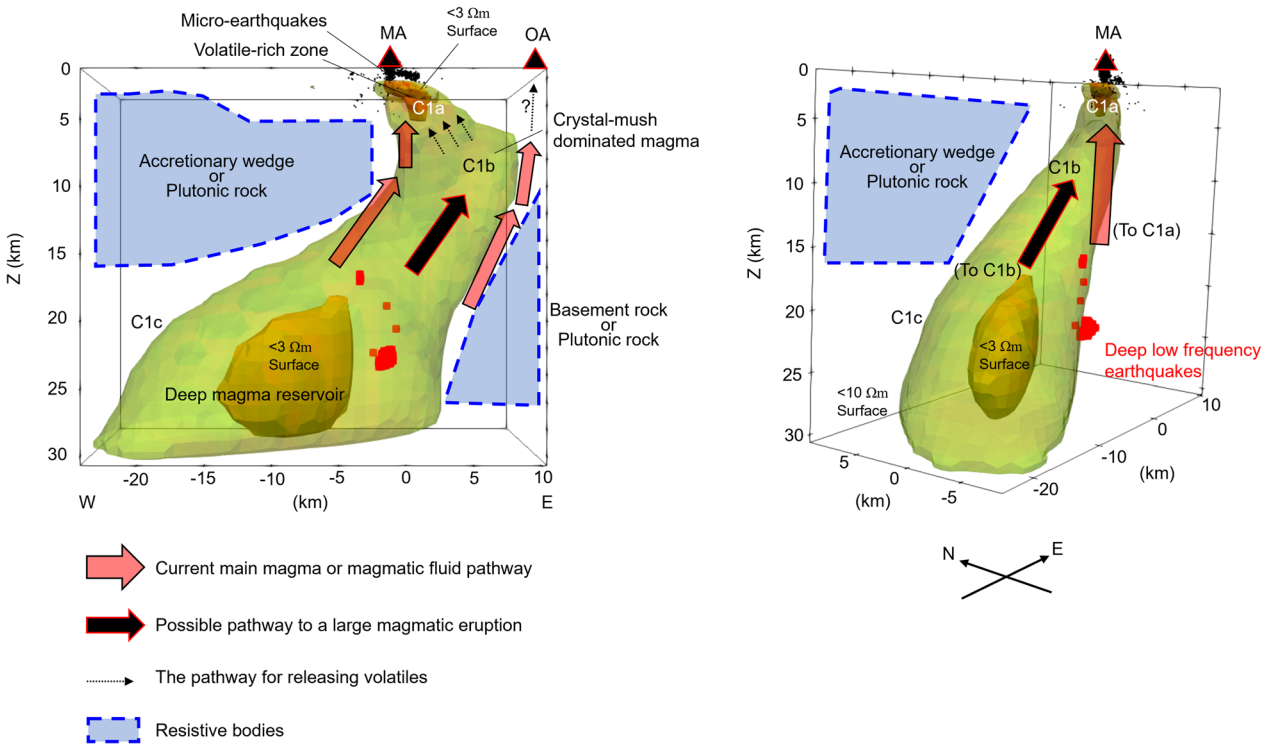


Fig. 10 3D view of the conductive column C1 and volcanic earthquakes showing iso-surfaces enclosing volumes of 3 Ωm (the inner zones around C1a and C1c) and 10 Ωm

Heise et al. 2024; Matsunaga et al. 2025). In contrast, a direct injection of magma from C1c into C1b may serve as an eruption-capable magma reservoir under appropriate conditions. Wada (1991) proposed a model in which basaltic magma is injected into a magma chamber containing dacitic magma. Following this concept, we interpret the lower part (C1c) as basaltic magma and the upper part (C1b) as dacitic magma.

C1b may consist of multiple interconnected magma systems. The petrological characteristics of the erupted material that formed the Akan Caldera suggest that the material was not derived from a single, large magma reservoir, but rather from multiple, compositionally diverse magma sources (Hasegawa et al. 2022). A comparison between the resistivity structure and gravity anomaly map (Hasegawa et al. 2009) shows that low-gravity anomalies—interpreted as past caldera-forming eruption centers—are distributed along the edges and in the central part of C1b (Fig. S9). These observations indicate that individual magma pathways may exist within C1b, both centrally and peripherally, each potentially leading to separate eruptions. Although most eruptive groups of Akan pyroclastic deposits (APD) are smaller than VEI 6 (< 10 km^3 DRE), the largest eruptive group had a volume exceeding 50 km^3 DRE (Hasegawa et al. 2022). The estimated volume of C1b exceeds approximetely 500 km^3 and its melt volume is estimated at 50–125 km^3 (see the liquid fraction in Sect. 4.1.1 and Fig. S8). Therefore, we assume that eruptions could be supplied solely by the magma stored in C1b. Such large eruptions may be triggered by direct magma injection from C1c and the associated remobilization of melt lenses and crystal mush within C1b.

A sill-shaped pressure source is located at the top of C1b (Fig. 8). Therefore, the ground inflation observed from 2016 to 2017 is caused by magma intrusion stored within C1b. However, it remains unclear whether the magma intruded from the central part of C1b or from its edges. Further observation data and studies on the detailed temporal evolution of the sill intrusion and earthquake hypocenters are needed to clarify the intrusion pathway. Previous studies on other volcanoes have shown a relationship between resistivity structures and crustal deformation sources, with many cases showing that spherical pressure sources correspond to the tops of conductive bodies (e.g., Azumayama; Ichiki et al. 2021; Kusatsu–Shirane; Matsunaga et al. 2022). In contrast, the top flattened shape of C1b differs from that of the subvertical conductive columns typically found beneath caldera volcanoes (Kelbert et al. 2012; Ichihara et al. 2013; Ogawa et al. 2014; Hata et al. 2018; Matsushima et al. 2020; Bertrand et al. 2022) and active volcanoes (Samrock et al. 2018; Hill et al. 2022; Aizawa et al. 2022a; Heise et al. 2024). These observations suggest that the Akan Caldera may possess a unique magma plumbing system centered on C1b, which can store a large volume of magma.

We interpret C1a as a volatile-rich zone formed by a combination of magmatic fluids discharged from the crystal mush magma in C1b and magmatic fluids migrating along the edges of C1b. Since C1b and C1a are likely connected, volatiles released from the crystal mush magma in C1b are probably supplied to the hydrothermal system in C1a. Additionally, fluids ascending along the edges of C1b may feed into C1a.

C1b and C1c are offset laterally but appear to be connected. Laterally offset magma reservoirs have been proposed in many volcanic regions (Lerner et al. 2020). One possible explanation is that older, solidified magma bodies (plutonic rocks) obstruct the vertical ascent of the current magma (Aizawa et al. 2009, 2022a; Usui et al. 2017; Bedrosian et al. 2018). This type of top–down control may also be applicable to the caldera. As shown in Figs. 8 and 10, a large resistive body (RW) is located above the deeper conductive zone (C1c). This resistive body causes the lateral offset between the deep basaltic reservoir (C1c) and the shallow dacitic crystal mush reservoir (C1b).

Specifically, this study clarifies the spatial relationship between ground deformation and the magma plumbing system in the caldera. Large-scale magmatic-hydrothermal systems can absorb magma intrusions from deeper sources and undergo multiple episodes of unrest, such as ground deformation, prior to eventual eruption (Acocella et al. 2015). Due to their large size and complexity, magma plumbing systems that can produce VEI 7 class eruptions (Cashman and Giordano 2014; Cashman et al. 2017) can easily pause or stall during magma ascent from depth before reaching the surface (Newhall et al. 2018). The post-caldera volcanoes are distributed along C1b in the Akan Caldera. This suggests that post-caldera eruptions may be driven by the persistence or rejuvenation of a magma reservoir after caldera formation. Future studies that combine the formation ages of post-caldera volcanoes with magma plumbing system models, constrained by petrological and geophysical data, will provide a more comprehensive understanding of the mechanisms underlying caldera-forming and post-caldera eruptions.

5 Conclusion

We conducted BBMT surveys around the Akan Caldera and revealed the subsurface resistivity structure through 3D inversion, enabling us to image the underlying magma plumbing system. The 3D resistivity model identified an inclined conductive column (C1) and a shallow conductive layer (CM) beneath the summit crater of Mt. Meakandake. The deformation sources and earthquake

hypocenters, including DLFEs, are located near the C1 edges. The results show that C1 is a key component of the caldera's magma plumbing system. The complex geometry of C1 was also analyzed by dividing it into three distinct parts to better understand magma/fluid movement. As a result, we propose that the three regions within C1 contribute to the volcanic activity within the Akan Caldera. These include (C1a: 2–5 km depth, ~ 10 km^3): a volatile-rich zone beneath Mt. Meakandake, (C1b: 3–15 km depth, ~ 500 km^3): a dacitic crystal mush magma reservoir acting as both a storage zone and a conduit for fluid transfer from deeper sources, and (C1c: > 15 km depth, ~ 4500 km^3): a segment of deep basaltic magma reservoir beneath the caldera. Magmatic fluids are likely supplied from the deeper western source (C1c), which is currently rising preferentially along the edges of C1. These edges are also closely associated with volcanic and seismic activity, suggesting that they play a central role in the control of dynamic processes within the caldera. In contrast, a direct injection of magma from C1c into C1b could remobilize the melt lenses and crystal mush within C1b, potentially culminating in a large magmatic eruption.

The main finding of this study is the identification of two distinct conductive bodies, C1b and C1c, beneath the central part of the Akan Caldera. These features were not clearly imaged in previous studies (Inoue et al. 2022). For the first time, we propose a magma reservoir structure that may be directly linked to the eruptive activity of the Akan Caldera. The 3D resistivity structure also provides a plausible magma pathway and clarifies the spatial relationship between unusual ground inflation events and underlying magmatic system. In conclusion, this study suggests that the different segments of the large conductive anomaly C1 play distinct geological roles. Our findings offer new insights into the magma plumbing system beneath the Akan Caldera and contribute to a better understanding of the mechanisms that drive its volcanic activity. In addition, the post-caldera volcano that most recently produced a caldera-forming eruption approximately 200 ka have been revealed to host a large magma reservoir in the subsurface. This finding suggests that the volume of magma stored beneath the volcano greatly exceeds the volume erupted at the surface.

Abbreviations

VEI	Volcanic Explosivity Index
APDs	Akan pyroclastic deposits
DRE	Dense rock equivalent
ka	Kilo annum
MT	Magnetotelluric
BBMT	Broadband magnetotelluric
AMT	Audio-frequency magnetotelluric
1D	One-dimensional
2D	Two-dimensional
3D	Three-dimensional
MA	Mt. Meakandake
OA	Mt. Oakandake
POQ	Phase out-of-quadrant
JMA	Japan Meteorological Agency
RMS	Root Mean Square
BSL	Below Sea Level

Supplementary Information

The online version contains supplementary material available at https://doi.org/10.1186/s40623-026-02398-8.

Additional file 1.

Additional file 2.

Acknowledgements

We are grateful of Prof. M. Uyeshima of University of Tokyo and Associate Prof. W. Kanda of Institute of Science Tokyo for the instrumental supports (ERI JURP 2020-F2-04, 2021-F2-04, 2022-F2-04). Audio-magnetotelluric (AMT) data in the summit area were provided by the National Institute of Advanced Industrial Science and Technology (AIST) and the Japan Meteorological Agency (JMA). The hypocenter data were provided by the Sapporo Regional Headquarters, JMA. We plotted the hypocenter data of deep low-frequency earthquakes of Kurihara and Obara (2021). We used GMT software (Wessel & Smith 1998) and Matplotlib (Hunter 2007) to draw some of the figures. We gratefully thank the editor, Takahiro Ohkura and anomalous reviewers for their valuable comments that significantly improved the manuscript. We express our thanks to Prof. K. Suzuki, M. Takada, A. Suzuki, K. Okada, R. Ito, Y. Iwama, K. Shibuya, A. Narita, K. Aoyama, T. Ugo, K. Kojima, T. Tashiro and R. Watatani of Hokkaido University, H. Koike, S. Horikawa, M. Kuroda and T. Ejiri of Nagoya University, S. Aniya, A. Okubo, K. Nakamura of Kyu-shu University, S. Kaneko of Chiba University for their supports in the fieldwork. We are grateful to Geothermal Energy Research & Development Co., Ltd for the reference data for remote reference processing. This work was supported by the Ministry of Education, Culture, Sports, Science and Technology of Japan (MEXT) under its Earthquake and Volcano Hazards Observation and Research Program, and Integrated Program for Next Generation Volcano Research and Human Resource Development.

Author contributions

TI, TH, KA and HI contributed to the study conceptualization, MT observations and discussion. TI analyzed the MT data. TI carried out the 3D modeling and visualization. TI and KA drafted the original manuscript. TH, KA and HI reviewed and helped finalizing the manuscript. YY acquired and analyzed the data in 2010 MT data. TH, KA, HI, RT and YY assisted with the interpretation. All authors read and approved the final manuscript.

Funding

This research was supported by the Ministry of Education, Culture, Sports, Science and Technology of Japan (MEXT) under its Earthquake and Volcano Hazards Observation and Research Program, and Integrated Program for Next Generation Volcano Research and Human Resource Development. This research was supported by Hokkaido University, Kyushu University and National Institute of Advanced Industrial Science and Technology.

Data availability

MT data are available from Tomohiro Inoue on reasonable request. The final resistivity structure is uploaded on web server of Japan Volcanological Data Network (https://jvdn.bosai.go.jp/app/pages/index.html?root=anyFileEdit&id=dd347304-6932-4d15-9ac4-eb7f018d4a15) (user registration required).

Declarations

Ethics approval and consent to participate

Not applicable.

Consent for publication

Not applicable.

Competing interests
The authors declare that they have no competing interests.

Author details
[1]Department of Natural History Sciences, Graduate School of Science, Hokkaido University, N10W8, Kita-ku, Sapporo, Hokkaido 060-0810, Japan. [2]Institute of Seismology and Volcanology, Faculty of Science, Kyushu University, 744 Motooka, Nishi-ku, Fukuoka 819-0385, Japan. [3]Present Address: National Institute of Advanced Industrial Science and Technology (AIST), Geological Survey of Japan, Higashi 1-1-1, Tsukuba, Japan. [4]Institute of Seismology and Volcanology, Faculty of Science, Hokkaido University, N10W8, Kita-ku, Sapporo, Hokkaido 060-0810, Japan. [5]Earthquake and Volcano Research Center, Graduate School of Environmental Studies, Nagoya University, Furo-Cho, Chikusa-Ku, Nagoya 464-8601, Japan. [6]Renewable Energy Advanced Research Center, National Institute of Advanced Industrial Science and Technology (AIST), Machiikedai 2-2-9, Koriyama, Fukushima 963-0928, Japan.

Received: 12 September 2025 Accepted: 10 February 2026
Published online: 16 March 2026

References

Acocella V, Di Lorenzo R, Newhall C, Scandone R (2015) An overview of recent (1988 to 2014) caldera unrest: knowledge and perspectives. Rev Geophys 53(3):896–955. https://doi.org/10.1002/2015RG000492

Aizawa K, Ogawa Y, Ishido T (2009) Groundwater flow and hydrothermal systems within volcanic edifices: delineation by electric self-potential and magnetotellurics. J Geophys Res Solid Earth. https://doi.org/10.1029/2008JB005910

Aizawa K, Koyama T, Hase H, Uyeshima M, Kanda W, Utsugi M, Yoshimura R, Yamaya Y, Hashimoto T, Yamazaki K, Komatsu S, Watanabe A, Miyakawa K, Ogawa Y (2014) Three-dimensional resistivity structure and magma plumbing system of the Kirishima Volcanoes as inferred from broadband magnetotelluric data. J Geophys Res Solid Earth 119(1):198–215. https://doi.org/10.1002/2013JB010682

Aizawa K, Utsugi M, Kitamura K, Koyama T, Uyeshima M, Matsushima N, Takakura S, Inagaki H, Saito H, Fujimitsu Y (2022a) Magmatic fluid pathways in the upper crust: insights from dense magnetotelluric observations around the Kuju Volcanoes, Japan. Geophys J Int 228:755–772. https://doi.org/10.1093/gji/ggab368

Aizawa K, Muramatsu D, Matsushima T, Koyama T, Uyeshima M, Nakao S (2022b) Phreatic volcanic eruption preceded by observable shallow groundwater flow at Iwo-Yama, Kirishima Volcanic Complex, Japan. Commun Earth Environ 3(1):187. https://doi.org/10.1038/s43247-022-00515-5

Aizawa K, Yamamoto Y, Wakabayashi A, Muramatsu D, Aniya S, Tanabe H, Fujita S, Azusa S, Koyama T, Shiozaki I, Ichiki M (2025) Three-dimensional resistivity structure beneath Beppu and Yufuin geothermal fields imaged by dense broad-band magnetotelluric observations. Earth Planets Space 77:159. https://doi.org/10.1186/s40623-025-02291-w

Aizawa K, Muramatsu D, Tsukamoto K, Teguri Y, Koyama T, Utsugi M, Kanda W, Inomata T, Shigematsu H, Shimizu H (2026) Trans-crustalbr/magma plumbing system of Kirishima volcanic complex as inferred from dense broad-band magnetotelluric observations. Earth Planets Space. https://doi.org/10.1186/s40623-026-02390-2

Aoyama H, Oshima H (2015) Precursory tilt changes of small phreatic eruptions of Meakan-dake volcano, Hokkaido, Japan, in November 2008. Earth Planets Space 67:119. https://doi.org/10.1186/s40623-015-0289-9

Bachmann O, Bergantz G (2008) The magma reservoirs that feed supereruptions. Elements 4(1):17–21. https://doi.org/10.2113/GSELEMENTS.4.1.17

Bedrosian PA, Peacock JR, Bowles-Martines E, Schultz A, Hill GJ (2018) Crustal inheritance and a top-down control on arc magmatism at Mount St Helens. Nat Geosci 11:865–870. https://doi.org/10.1038/s41561-018-0217-2

Bertrand E, Kannberg P, Caldwell T, Heise W, Constable S, Scott B, Bannister S, Kilgour G, Bennie S, Hart R, Palmer N (2022) Inferring the magmatic roots of volcano-geothermal systems in the Rotorua Caldera and Okataina Volcanic Centre from magnetotelluric models. J Volcanol Geotherm Res. https://doi.org/10.1016/j.jvolgeores.2022.107645

Bowles-Martinez E, Schultz A (2020) Composition of magma and characteristics of the hydrothermal system of Newberry Volcano, Oregon, from magnetotellurics. Geochem Geophys Geosyst. https://doi.org/10.1029/2019GC008831

Caldwell TG, Bibby HM, Brown C (2004) The magnetotelluric phase tensor. Geophys J Int 158:457–469. https://doi.org/10.1111/j.1365-246X.2004.02281.x

Cashman KV, Giordano G (2014) Calderas and magma reservoirs. J Volcanol Geotherm Res 288:28–45. https://doi.org/10.1016/j.jvolgeores.2014.09.007

Cashman KV, Sparks RSJ, Blundy JD (2017) Vertically extensive and unstable magmatic systems: a unified view of igneous processes. Science 355(6331):eaag3055. https://doi.org/10.1126/science.aag3055

Chave AD, Thomson DJ (2004) Bounded influence magnetotelluric response function estimation. Geophys J Int 157:988–1006. https://doi.org/10.1111/j.1365-246X.2004.02203.x

Cordell D, Unsworth MJ, Lee B, Díaz D, Bennington NL, Thurber CH (2020) Integrating magnetotelluric and seismic images of silicic magma systems: a case study from the Laguna del Maule Volcanic Field, central Chile. J Geophys Res Solid Earth 125(11):e2020JB020459. https://doi.org/10.1029/2020JB020459

Di Giuseppe MG, Isaia R, Troiano A (2023) Three-dimensional magnetotellruric modeling of Vulcano Island (Eolie, Italy) and its implications for understanding recent volcanic unrest. Sci Rep 13(1):16458. https://doi.org/10.1038/s41598-023-43828-x

Egbert GD (1990) Comments on "Concerning dispersion relations for the magnetotelluric impedance tensor" by E. Yee and K.V. Paulson. Geophys J Int 102:1–8. https://doi.org/10.1111/j.1365-246X.1990.tb00525.x

Egbert GD, Kelbert A (2012) Computational recipes for electromagnetic inverse problems. Geophys J Int 189:251–267. https://doi.org/10.1111/j.1365-246X.2011.05347.x

Gaillard F, Marziano GI (2005) Electrical conductivity of magma in the course of crystallization controlled by their residual liquid composition. J Geophys Res 110:B06204. https://doi.org/10.1029/2004JB003282

Gamble TD, Goubau WM, Clarke J (1979) Magnetotelluric with a remote magnetic reference. Geophys 44:53–68. https://doi.org/10.1190/1.1440923

Geospatial Information Authority of Japan (2018) Crustal Deformations around Meakan Volcano. Report of the Coordinating Committee for Prediction of Volcanic Eruptions 128:5–19

Guo X, Zhang L, Behrens H, Ni H (2016) Probing the status of felsic magma reservoirs: constraints from the P-T–H2O dependences of electrical conductivity of rhyolitic melt. Earth Planet Sci Lett 433:54–62. https://doi.org/10.1016/j.epsl.2015.10.036

Guo X, Li B, Ni H, Mao Z (2017) Electrical conductivity of hydrous andesitic melts pertinent to subduction zones. J Geophys Res Solid Earth. https://doi.org/10.1002/2016JB013524

Hasegawa T, Nakagawa M (2016) Large scale explosive eruptions of Akan volcano, eastern Hokkaido, Japan: a geological and petrological case study for establishing tephro-stratigraphy and-chronology around a caldera cluster. Quat Int 397:39–51. https://doi.org/10.1016/j.quaint.2015.07.058

Hasegawa T, Yamamoto A, Kamiyama H, Nakagawa M (2009) Gravity structure of Akan composite caldera, eastern Hokkaido, Japan: application of lake water corrections. Earth Planets Space 61:933–938. https://doi.org/10.1186/BF03353205

Hasegawa T, Nakagawa M, Kishimoto H (2012) The eruption history and silicic magma systems of caldera-forming eruptions in eastern Hokkaido, Japan. J Mineral Petrol Sci 107(1):39–43. https://doi.org/10.2465/jmps.111020h

Hasegawa T, Nakagawa M, Kamiyama H, Yamamoto A (2022) Geological, geophysical, and geochemical constraints on the time-space evolution of Akan composite caldera, Hokkaido, Japan. Front Earth Sci 10:953152. https://doi.org/10.3389/feart.2022.953152

Hashimoto TM, Aizawa K, Hayashida Y, Yuasa Y, Matsushima T, Yamamoto Y, Tsukamoto K, Miyano K, Matsumoto S, Shimizu H (2020) Joint seismological–magnetotelluric investigation of shallow and implosive non-DC and DC earthquakes beneath the gravitationally unstable Heisei-Shinzan Lava Dome, Unzen Volcano, Japan. J Volcanol Geotherm Res 406:107066. https://doi.org/10.1016/j.jvolgeores.2020.107066

Hashin Z, Shtrikman S (1962) A variational approach to the theory of the effective magnetic permeability of multiphase materials. J Appl Phys 33(10):3125–3131. https://doi.org/10.1063/1.1728579

Hata M, Matsushima N, Takakura S, Utsugi M, Hashimoto T, Uyeshima M (2018) Three-dimensional electrical resistivity modeling to elucidate the crustal magma supply system beneath Aso caldera, Japan. J Geophys Res Solid Earth 123(8):6334–6346. https://doi.org/10.1029/2018JB015951

Heise W, Pous J (2003) Anomalous phases exceeding 90º in magnetotellurics: anisotropic model studies and a field example. Geophys J Int 155(1):308–318. https://doi.org/10.1046/j.1365-246X.2003.02050.x

Heise W, Bannister S, Williams CA, McGavin P, Caldwell TG, Bertrand EA, Usui Y, Kilgour G (2024) Magmatic priming of a phreatic eruption sequence: the 2012 Te Maari eruptions at Mt. Tongario (New Zealand) imaged by magneotellurics and seismicity. Geophys J Int 236:1848–1862. https://doi.org/10.1093/gji/ggae022

Hill GJ, Wannamaker PE, Maris V, Stodt JA, Kordy M, Unsworth MJ, Bedrosian PA, Wallin EL, Uhlmann DF, Ogawa Y, Kyle P (2022) Trans-crustal structural control of CO2-rich extensional magmatic systems revealed at Mount Erebus Antarctica. Nat Commun 13(1):2989. https://doi.org/10.1038/s41467-022-30627-7

Hogg C, Kiyan D, Rath V, Byrdina S, Vandemeulebrouck J, Revil A, Viverios F, Carmo R, Silva C, Ferreira T (2018) 3-D interpretation of short-period magnetotelluric data at Furnas Volcano, Azores Islands. Geophys J Int 213(1):371–386. https://doi.org/10.1093/gji/ggx512

Hunter J (2007) Matplotlib: a 2D graphics environment. Comput Sci Eng 9:90–95. https://doi.org/10.1109/MCSE.2007.55

Ichihara H, Mogi T (2009) A realistic 3-D resistivity model explaining anomalous large magnetotelluric phases: the L-shaped conductor model. Geophys J Int 179(1):14–17. https://doi.org/10.1111/j.1365-246X.2009.04310.x

Ichihara H, Mogi T, Yamaya Y (2013) Three-dimensional resistivity modelling of a seismogenic area in an oblique subduction zone in the western Kurile arc: constraints from anomalous magnetotelluric phases. Tectonophysics 603:114–122. https://doi.org/10.1016/j.tecto.2013.05.020

Ichihara H, Mogi T, Satoh H, Yamaya Y (2019) Electrical resistivity modeling around the Hidaka collision zone, northern Japan: regional structural background of the 2018 Hokkaido Eastern Iburi earthquake (Mw 6.6). Earth Planets Space 71:100. https://doi.org/10.1186/s40623-019-1078-7

Ichiki M, Kaida T, Nakayama T, Miura S, Yamamoto M, Morita Y, Uyeshima M (2021) Magma reservoir beneath Azumayama Volcano, NE Japan, as inferred from a three-dimensional electrical resistivity model explored by means of magnetotelluric method. Earth Planets Space 73:150. https://doi.org/10.1186/s40623-021-01451-y

Inoue T, Hashimoto T (2024) The inclined conductive column effect: a new simple model for magnetotelluric anomalous phases. Geophys J Int 238(3):1825–1839. https://doi.org/10.1093/gji/ggae252

Inoue T, Hashimoto T, Tanaka R, Yamaya Y (2022) A broadband magnetotelluric survey for Mt. Meakandake volcano with special attention to the unrest during 2016–2017. Earth Planets Space 74(1):114. https://doi.org/10.1186/s40623-022-01673-8

Isaia R, Troiano A, Di Giuseppe MG, De Paola C, Gottsmann J, Pagliara F, Smith VC, Stock MJ (2025) 3D magnetotelluric imaging of a transcrustal magma system beneath the Campi Flegrei caldera, southern Italy. Commun Earth Environ 6(1):213. https://doi.org/10.1038/s43247-025-02185-5

Japan Meteorological Agency (2013) National catalogue of the active volcanoes in Japan, 4th ed. Japan Meteological Agency, Tokyo

Jones AG, Kurtz RD, Oldenburg DW, Boerner DE, Ellis R (1988) Magnetotelluric observations along the LITHOPROBE southeastern Canadian Cordilleran transect. Geophys Res Lett 15(7):677–680. https://doi.org/10.1029/GL015i007p00677

Kanda W, Utsugi M, Takakura S, Inoue H (2019) Hydrothermal system of the active crater of Aso volcano (Japan) inferred from a three-dimensional resistivity structure model. Earth Planets Space 71(1):37. https://doi.org/10.1186/s40623-019-1017-7

Kelbert A, Egbert GD, DeGroot-Hedlin C (2012) Crust and upper mantle electrical conductivity beneath the Yellowstone Hotspot Track. Geology. https://doi.org/10.1130/G32655.1

Kelbert A, Mequbel N, Egbert GD, Tandon K (2014) ModEM: a modular system for inversion of electromagnetic geophysical data. Compute Geos 66:40–53. https://doi.org/10.1130/G32655.1

Komori S, Takakura S, Mitsuhata Y, Yokota T, Uchida T, Makino M, Kato Y, Yamamoto K (2024) Three-dimensional resistivity structure in Toya caldera region, Southwest Hokkaido, Japan—constraints on magmatic and geothermal activities. Geophysics 89(1):B31–B50. https://doi.org/10.1190/geo2022-0558.1

Kurihara R, Obara K (2021) Spatiotemporal characteristics of relocated deep low-frequency earthquakes beneath 52 volcanic regions in Japan over an analysis period of 14 years and 9 months. J Geophys Res Solid Earth 126(10):e2021JB022173. https://doi.org/10.1029/2021JB022173

Kuritani T, Sato E, Wada K, Matsumoto A, Nakagawa M, Zhao D, Shimizu K, Ushikubo T (2021) Conditions of magma generation at the Me-akan volcano, northern Japan. J Volcanol Geotherm Res 417:107323. https://doi.org/10.1016/j.jvolgeores.2021.107323

Laumonier M, Gaillard F, Sifre D (2015) The effect of pressure and water concentration on the electrical conductivity of dacitic melts: implication for magnetotelluric imaging in subduction areas. Chem Geol 418:66–76. https://doi.org/10.1016/j.chemgeo.2014.09.019

Lerner AH, O'Hara D, Karlstorm L, Ebmeier SK, Anderson KR, Hurwitz S (2020) The prevalence and significance of offset magma reservoirs at arc volcanoes. Geophys Res Lett. https://doi.org/10.1029/2020GL087856

Lindsey NJ, Kaven JO, Davatzes N, Newman GA (2016) Compartmentalization of the Coso East Flank geothermal field imaged by 3-D full-tensor MT inversion. Geophys J Int. https://doi.org/10.1093/gji/ggw408

Mannen K, Abe Y, Daita Y, Doke R, Harada M, Kikugawa G, Honma N, Miyashita Y, Yukutake Y (2021) Volcanic unrest at Hakone volcano after 2015 eruption: Reactivation of a ruptured hydrothermal system? Earth Planets Space 73:80. https://doi.org/10.1186/s40623-021-01387-3

Matsunaga Y, Kanda W, Koyama T, Takakura S, Nishizawa T (2022) Large-scale magmatic-hydrothermal system of Kusatsu-Shirane Volcano, Japan, revealed by broadband magnetotellurics. J Volcanol Geotherm Res 429:107600. https://doi.org/10.1016/j.jvolgeores.2022.107600

Matsunaga K, Aizawa K, Asamori K, Ogawa H, Utsugi M, Yoshimura R, Yamazaki K, Uchida K, Matsushima T, Inoue T, Yonemori K, Shigematsu H (2025) Three-dimensional resistivity structure and its relationship to the rupture of the 1997 Kagoshima earthquake doublet (Mw 6.1 and 6.0), Japan. Tectonophysics. https://doi.org/10.1016/j.tecto.2025.230880

Matsushima N, Utsugi M, Takakura S, Yamasaki T, Hata M, Hashimoto T, Uyeshima M (2020) Magmatic-hydrothermal system of Aso Volcano, Japan, inferred from electrical resistivity structures, Earth. Planet Space Sci 72:57. https://doi.org/10.1186/s40623-020-01180-8

Melnik O, Lyakhovsky V, Shapiro NM, Galina N, Bergal-Kuvikas O (2020) Deep long period volcanic earthquakes generated by degassing of volatile-rich basaltic magmas. Nat Commun 11(1):3918. https://doi.org/10.1038/s41467-020-17759-4

Minami Y, Nakagawa M, Sato E, Wada K, Ishizuka Y (2021) Eruptive history during the last 1,000 years at Ponmachineshiri in Meakandake volcano, eastern Hokkaido, Japan. Volcanol Soc Jpn 66(3):211–227. https://doi.org/10.18940/kazan.66.3_211. (**in Japanese with English abstract**)

Mogi T, Yamaya Y, Hashimoto T, Akita F, Shibata T, Takahashi T, Tamura S (2011) MT survey in Akanko Hot Springs. In: The proceedings of Society of Exploration Geophysicsts of Japan 125:147–150.

Narita S, Ozawa T, Aoki Y, Shimada M, Furuya M, Takada Y, Murakami M (2020) Precursory ground deformation of the 2018 phreatic eruption on Iwo-Yama volcano, revealed by four-dimensional joint analysis of airborne and spaceborne InSAR. Earth Planets Space 72(1):145. https://doi.org/10.1186/s40623-020-01280-5

New Energy and Industrial Technology Development Organization (1992) Report of the Geothermal Development Promotion Survey (Akan), pp. 639–769, https://geothermal.jogmec.go.jp/report/nedo/file/6.pdf (**in Japanese**)

Newhall C, Self S, Robock A (2018) Anticipating future volcanic explosivity index (VEI) 7 eruptions and their chilling impacts. Geosphere 14(2):572–603. https://doi.org/10.1130/GES01513.1

Ogawa Y, Ichiki M, Kanda W, Mishina M, Asamori K (2014) Three-dimensional magnetotelluric imaging of crustal fluids and seismicity around Naruko volcano, NE Japan. Earth Planets Space. https://doi.org/10.1186/s40623-014-0158-y

Ogiso M, Yomogida K (2021) Estimation of relative source locations from seismic amplitude: application to earthquakes and tremors at Meakandake vocano, eastern Hokkaido, Japan. Earth Planets Space 73:29. https://doi.org/10.1186/s40623-021-01366-8

Ohba T, Yaguchi M, Tsunogai U, Ito M, Shingubara R (2021) Behavior of magmatic components in fumarolic gases related to the 2018 phreatic eruption at Ebinokogen Ioyama volcano, Kirishima Volcanic Group, Kyushu, Japan. Earth Planets Space 73:1–17. https://doi.org/10.1186/s40623-021-01405-4

Parkinson WD (1962) The influence of continents and oceans on geomagnetic variations. Geophys J Int 6:441–449. https://doi.org/10.1111/j.1365-246X.1962.tb02992.x

Peacock JR, Mangan MT, McPhee D, Ponce DA (2015) Imaging the magmatic system of Mono Basin, California, with magnetotellurics in three dimensions. J Geophys Res Solid Earth 120(11):7273–7289. https://doi.org/10.1002/2015JB012071

Peacock JR, Mangan MT, McPhee D, Wannamaker PE (2016) Three-dimensional electrical resistivity model of the hydrothermal system in Long Valley Caldera, California, from magnetotellurics. Geophys Res Lett. https://doi.org/10.1002/2016GL069263

Piña-Varas P, Dentith M (2018) Magnetotelluric data from the Southeastern Capricorn Orogen, Western Australia: an example of widespread out-of-quadrant phase responses associated with strong 3-D resistivity contrasts. Geophys J Int 212:1022–1032. https://doi.org/10.1093/gji/ggx459

Piña-Varas P, Ledo J, Queralt P, Marcuello A, Bellmunt F, Hidalgo R, Messeiller M (2014) 3-D magnetotelluric exploration of Tenerife geothermal system (Canary Islands, Spain). Surv Geophys 35(4):1045–1064. https://doi.org/10.1007/s10712-014-9280-4

Raju K, Patro PK (2023) Modelling of subsurface geological structure related to anomalous magnetotelluric phase data exceeding 90º in Central India. Geophys J Int 235:1671–1680. https://doi.org/10.1093/gji/ggad318

Raju K, Patro PK, Borah UK, Srivasta S, Reddy KC (2022) Evolution of eastern segment of the Central India Tectonic Zone: an insight from a magnetotelluric study. Geophys J Int 230:272–287. https://doi.org/10.1093/gji/ggac073

Samrock F, Grayver AV, Eysteinsson H, Saar MO (2018) Magnetotelluric image of transcrustal magmatic system beneath the Tulu Moye geothermal prospect in the Ethiopian Rift. Geophys Res Lett 45(23):12–847. https://doi.org/10.1029/2018GL080333

Scarlato P, Poe BT, Freda C, Gaeta M (2004) High-pressure and high-temperature measurements of electrical conductivity in basaltic rocks from Mount Etna, Sicily, Italy. J Geophys Res Solid Earth. https://doi.org/10.1029/2003JB002666

Shinohara H, Matsushima N, Kazahaya K, Ohwada M (2011) Magma-hydrothermal system interaction inferred from volcanic gas measurements obtained during 2003-2008 at Meakandake volcano, Hokkaido, Japan. Bull Volcanol 73:409–421. https://doi.org/10.1007/s00445-011-0463-2

Stix J, de Moor JM (2018) Understanding and forecasting phreatic eruptions driven by magmatic degassing. Earth Planets Space 70:1–19. https://doi.org/10.1186/s40623-018-0855-z

Takahashi K, Takakura S, Matsushima N, Fujii I (2018) Relationship between volcanic activity and shallow hydrothermal system at Meakandake volcano, Japan, inferred from geomagnetic and audio-frequency magnetotelluric measurements. J Volcanol Geotherm Res 349:351–369. https://doi.org/10.1016/j.jvolgeores.2017.11.019

Takahashi R, Ogino T, Ohmori K, Murayama Y (2023) Chemical and thermal changes in hot spring waters and fumarolic gases related to volcanic unrest at Meakandake volcano, Japan: results of long-term geochemical monitoring from 1986 to 2022. J Volcanol Geotherm Res 443:107934. https://doi.org/10.1016/j.jvolgeores.2023.107934

Tamada J, Nakagawa M (2009) Eruption history of Oakan volcano, eastern, Hokkaido Japan. Volcanol Soc Jpn 54:147–162. https://doi.org/10.18940/kazan.54.4_147

Terada A, Kanda W, Ogawa Y, Yamada T, Yamamoto M, Ohkura T, Aoyama H, Tsutsui T, Onizawa SY (2021) The 2018 phreatic eruption at Mt. Motoshirane of Kusatsu-Shirane volcano, Japan: eruption and intrusion of hydrothermal fluid observed by a borehole tiltmeter network. Earth Planets Space 73:1–17. https://doi.org/10.1186/s40623-021-01475-4

Triahadini A, Aizawa K, Hashimoto TM, Chiba K, Uchida K, Yamamoto Y, Miyano K, Muramatsu D, Aniya S, Okubo A, Kawamura Y (2023) Magma transport along structural boundaries in the upper crust: insights from broad-band magnetotelluric constraints on the structure beneath Unzen volcano, Japan. Geophys J Int 234(2):1268–1281. https://doi.org/10.1093/gji/ggad126

Tseng KH, Ogawa Y, Nurhasan Tank SB, Ujihara N, Honkura Y, Terada A, Usui Y, Kanda W (2020) Anatomy of active volcanic edifice at the Kusatsu-Shirane volcano, Japan, by magnetotellurics: hydrothermal implications for volcanic unrests. Earth Planets Space 72:1–11. https://doi.org/10.1186/s40623-020-01283-2

Tsukamoto K, Aizawa K, Chiba K, Kanda W, Uyeshima M, Koyama T, Utsugi K, Seki K, Kishita T (2018) Three-dimensional resistivity structure of Iwo-Yama volcano, kirishima volcanic complex, Japan: relationship to shallow seismicity, surface uplift, and a small phreatic eruption. Geophys Res Lett 45(23):12–821. https://doi.org/10.1029/2018GL080202

Ukawa M, Ohtake M (1987) A monochromatic earthquake suggesting deep-seated magmatic activity beneath the Izu-Ooshima Volcano, Japan. J Geophys Res Solid Earth 92(B12):12649–12663. https://doi.org/10.1029/JB092iB12p12649

Usui Y (2015) 3-D inversion of magnetotelluric data using unstructured tetrahedral elements: applicability to data affected by topography. Geophys J Int 202:828–849. https://doi.org/10.1093/gji/ggv186

Usui Y, Ogawa Y, Aizawa K, Kanda W, Hashimoto T, Koyama T, Yamaya Y, Kagiyama T (2017) Three-dimensional resistivity structure of Asama volcano revealed by data-space magnetotelluric inversion using unstructured tetrahedral elements. Geophys J Int 208(3):1359–1372. https://doi.org/10.1093/gji/ggw459

Usui Y, Uyeshima H, Hase H, Ichihara H, Aizawa K, Koyama T, Sakanaka S, Ogawa T, Yamaya Y, Nishitani T, Asamori K, Ogawa Y, Yoshimura R, Takakura S, Mishina M, Morita Y (2024) Three-dimensional electrical resistivity structure beneath a strain concentration area in the back-arc side of the northeastern Japan arc. J Geophys Res Solid Earth 129:e2023JB028522. https://doi.org/10.1029/2023JB028522

Wada K (1991) Mixing and evolution of magmas at Me-akan Volcano, eastern Hokkaido, Japan. Volcanol Soc Jpn 36:61–78. https://doi.org/10.18940/kazan.36.1_61. (**in Japanese with English abstract**)

Wada K, Ikegami H, Inaba T (1998) Chemical compositions of the rocks from Me-akan volcano eastern Hokkaido Japan: compositional variety of eruptive magmas. Rep Taisetsuzan Inst Sci 32:43–59. https://www.asa.hokkyodai.ac.jp/taisetsu/wp-content/uploads/2016/03/32_05.pdf **(in Japanese with English abstract)**

Wakana I, Kadono Y, Urabe J, Tamura Y, Suzuki Y, Yamada H, Oyama Y, Wada K, Hasegawa T, Ohara M (2023) Varying stages of ecological succession in lakes subdivided by volcanic eruptions at Akan Caldera, Japan. Hydrobiologia 850(18):3919–3933. https://doi.org/10.1007/s10750-023-05231-5

Watanabe N, Mogi T, Yamaya Y, Kitamura K, Asanuma H, Tsuchiya N (2022) Electrical conductivity of H_2O-NaCl fluids under supercritical geothermal conditions and implications for deep conductors observed by the magnetotelluric method. Geothermics 101:102361. https://doi.org/10.1016/j.geothermics.2022.102361

Weckmann U, Ritter O, Haak V (2003) A magnetotelluric study of the Damara Belt in Namibia: 2. MT phases over 90º reveal the internal structure of the Waterberg Fault/Omaru Lineament. Phys Earth Planet Inter 138(2):91–112. https://doi.org/10.1016/S0031-9201(03)00079-7

Wessel P, Smith WHF (1998) New, improved version of the Generic Mapping Tools released. EOS, Trans Am Geophys Un 79:579. https://doi.org/10.1029/98EO00426

Yamaya Y, Alanis PKB, Takeuchi A, Cordon JJM, Mogi T, Hashimoto T, Sasai Y, Nagao T (2013) A large hydrothermal reservoir beneath Taal Volcano (Philippines) revealed by magnetotelluric resistivity survey: 2D resistivity modeling. Bull Volcanol 75(7):729. https://doi.org/10.1007/s00445-013-0729-y

Yoshimura R, Ogawa Y, Yukutake Y, Kanda W, Komori S, Hase H, Goto T, Honda R, Harada M, Yamazaki T, Kamo M, Kawasaki S, Higa T, Suzuki T, Yasuda Y, Tani M, Usui Y (2018) Resistivity characterisation of Hakone volcano, Central Japan, by three-dimensional magnetotelluric inversion. Earth Planets Space 70(1):1–10. https://doi.org/10.1186/s40623-018-0848-y

Publisher's Note

Springer Nature remains neutral with regard to jurisdictional claims in published maps and institutional affiliations.